Monthly Notices of the ROYAL ASTRONOMICAL SOCIETY

MNRAS **542,** 960–981 (2025)
Advance Access publication 2025 July 14

https://doi.org/10.1093/mnras/staf1138

JADES and SAPPHIRES: galaxy metamorphosis amidst a huge, luminous emission-line region

Francesco D'Eugenio [1,2★] Jakob M. Helton [3] Kevin Hainline [3] Fengwu Sun [4] Roberto Maiolino [1,2,5] Pablo G. Pérez-González [6] Ignas Juodžbalis [1,2] Santiago Arribas [6] Andrew J. Bunker [7] Stefano Carniani [8] Emma Curtis-Lake [9] Eiichi Egami [3] Daniel J. Eisenstein [4] Benjamin D. Johnson [4] Brant Robertson [10] Sandro Tacchella [1,2] Christopher N. A. Willmer [3] Chris Willott [11] William M. Baker [12] A. Lola Danhaive [1,2] Qiao Duan [1,2] Yoshinobu Fudamoto [3,13] Gareth C. Jones [1,2] Xiaojing Lin [3] Weizhe Liu(刘伟哲) [3] Michele Perna [6] Dávid Puskás [1,2] Pierluigi Rinaldi [3] Jan Scholtz [1,2] Yang Sun [3] James A. A. Trussler [4] Hannah Übler [14] Giacomo Venturi [8] Christina C. Williams [15] and Yongda Zhu [3]

Affiliations are listed at the end of the paper

Accepted 2025 July 7. Received 2025 June 2; in original form 2025 March 15

ABSTRACT

We report the discovery of a remarkably large and luminous line-emitting nebula extending on either side of the Balmer-break galaxy JADES-GS-518794 at $z = 5.89$, detected with *James Webb Space Telescope* (*JWST*)/NIRCam imaging in [O III]λλ4959, 5007 and Hα and spectroscopically confirmed with NIRCam/wide-field slitless spectroscopy, thanks to the pure-parallel programme Slitless Areal Pure Parallel HIgh-Redshift Emission Survey. The end-to-end velocity offset is $\Delta v = 830 \pm 130$ km s^{-1}. Nebulae with such large sizes and high luminosities (25 pkpc diameter, $L_{[\mathrm{O\,III}]} = 1.2 \times 10^{10}$ L$_\odot$) are routinely observed around bright quasars, unlike JADES-GS-518794. With a stellar mass of $10^{10.1}$ M$_\odot$, this galaxy is at the knee of the mass function at $z = 6$. Its star formation rate declined for some time (10–100 Myr prior to observation), followed by a recent (10 Myr) upturn. This system is part of a candidate large-scale galaxy overdensity, with an excess of Balmer-break galaxies compared to the field (3σ). We discuss the possible origin of this nebula as material from a merger or gas expelled by an active galactic nucleus (AGN). The symmetry of the nebula, its bubble-like morphology, kinematics, high luminosity, and the extremely high equivalent width of [O III] together favour the AGN interpretation. Intriguingly, there may be a physical connection between the presence of such a large, luminous nebula and the possible metamorphosis of the central galaxy towards quenching.

Key words: galaxies: active – galaxies: evolution – galaxies: formation – galaxies: high-redshift – galaxies: jets.

1 INTRODUCTION

No known physical process other than accreting supermassive black holes (SMBHs) can release sufficient energy to curtail star formation in massive, central galaxies (Haehnelt, Natarajan & Rees 1998; Silk & Rees 1998; Binney 2004). Theoretical models and numerical simulations demonstrate that without this source of feedback, violent starbursts would bring forth a host of titanic galaxies which defy observations (stellar mass $M_\star \sim 10^{13}$ M$_\odot$; Bower, Benson & Crain 2012). Yet the precise mechanisms by which active galactic nuclei (AGNs) shape the star formation history (SFH) of galaxies are still unclear. Numerical simulations (e.g. Piotrowska et al. 2022) and observations (Terrazas et al. 2017; Bluck et al. 2022; Bluck, Piotrowska & Maiolino 2023) suggest that the protracted absence of star formation in galaxies (quiescence) is best predicted by SMBH mass, which we can interpret as a 'calorimeter' measuring time-integrated feedback from AGNs. Together with evidence of a systematic increase in stellar metallicity from star forming to quiescent galaxies (Peng, Maiolino & Cochrane 2015; Trussler et al. 2020; Baker et al. 2024; Looser et al. 2024a), the emerging scenario is that the energy released by SMBH accretion accumulates in the halo, which stops the cold gas accretion on to the central galaxy and thus prevents star formation (preventive feedback scenario).

This coherent picture has been recently challenged by new *James Webb Space Telescope* (*JWST*) observations of massive, quiescent galaxies at redshifts $z = 3$–7 (Carnall et al. 2023b, 2024; Weibel et al. 2025). The key challenges in the preventive-feedback scenario are the high number density of these quiescent systems (Carnall et al. 2023a; Valentino et al. 2023; Long et al. 2024; Nanayakkara et al. 2024, 2025; Baker et al. 2025a) and their rapid formation and quenching (Carnall et al. 2023b, 2024; Glazebrook et al. 2024; de Graaff et al.

★ E-mail: francesco.deugenio@gmail.com

2025; Turner et al. 2025; Weibel et al. 2025). By redshift $z = 3$, there is already evidence for the existence of quiescent, gas-depleted systems (Scholtz et al. 2024). While some models are more successful than others (Rennehan et al. 2024; Lagos et al. 2025; Remus & Kimmig 2025), some form of more powerful or more efficient AGN feedback seems required to match the observations (Xie et al. 2024). Ejective feedback may play an important role, as evidenced by direct observations of neutral-gas outflows with high mass loading ($z = 2.5$–3; Belli et al. 2024; D'Eugenio et al. 2024; Wu 2025), with an incidence of 30–40 per cent in the massive-galaxy population at $z = 1$–2.5 (Davies et al. 2024). Where these quiescent galaxies with outflows have deep observations at sub-mm wavelengths, no significant molecular gas is detected (with a molecular-gas to stellar mass fraction of less than 3 per cent; Scholtz et al. 2024), consistent with rapid gas removal (although gas consumption with no refuelling would also explain the lack of gas). Intriguingly, one of these outflows is observed in a galaxy without evidence of AGN (Valentino et al. 2025).

Though alluring, rapid quenching scenarios raise the issue of what are the star-forming progenitors of these early quiescent systems, because at $z = 7$–11, compact starbursts with star formation rates (SFRs) of several hundred $M_\odot$ yr^{-1} should be readily observable by *JWST* (e.g. Turner et al. 2025; Weibel et al. 2025), but currently remain unseen. At first glance, a captivating explanation is that these missing progenitors may be heavily dust obscured as the compact size of the quiescent galaxies and their high metal content are both conducive to severe dust attenuation. But even this explanation is not completely satisfactory: where are the transitional systems between the dust-obscured, metal-rich progenitor galaxies and their (relatively) dust free, quiescent descendants?

A possible solution to this conundrum is that during the transition phase, AGNs may have a high duty cycle, such that most progenitors are AGN hosts. Supporting evidence for this scenario comes from the discovery that some faint-quasar host galaxies have post-starburst spectral features, indicating a protracted lack of star formation (Onoue et al. 2024), but more statistics are needed to confirm this scenario. A number of transitioning progenitors may be hidden by dust-obscured AGNs (Banerji et al. 2015; Ross et al. 2015; Hamann et al. 2017; Wang et al. 2024), though there are claims that these systems may harbour ongoing star formation (Killi et al. 2024). Alternatively, the transition from dust-obscured star formation may be extremely rapid, shortening its visibility time. During this 'blowout' phase, one or more AGN events would destroy and/or remove most of the galaxy interstellar medium (ISM; Hopkins et al. 2008). Evidence for such a scenario comes from observations of extended emission-line regions around quasars (e.g. Marshall et al. 2023; Perna et al. 2023; Liu et al. 2024, 2025; Vayner et al. 2024; Zamora et al. 2024; Peng et al. 2025), including faint systems (Lyu et al. 2025). A fraction of this nebular emission could be due to satellite galaxies and their tidally disrupted ISM, because quasars may trace overdensities (e.g. Kashino et al. 2023; Wang et al. 2023b – but see Eilers et al. 2024 for a different view). However, a non-negligible part of the ionized gas in these extended nebulae may have originally been part of the ISM of the central galaxy before being expelled. This view is supported by the finding that the observed extended gas emission is metal-rich, as suggested by the presence of fast gas outflows in action in quasars and by the very high equivalent width (EW) of the emission lines which challenges the tidal-disruption and star formation interpretations (Lyu et al. 2025).

Recent observations of massive, quiescent galaxies at $z = 3$–4 show the presence of extended and metal-rich gas nebulae (D'Eugenio et al. 2024; Pérez-González et al. 2024) on scales of the circumgalactic medium (CGM) of these compact galaxies. However, it is still unclear if these CGM nebulae are due to mergers or to outflows (D'Eugenio et al. 2024), and if some of them are powered by *in situ* AGNs (Perna et al. 2025), or by an AGN from the central galaxy (Pérez-González et al. 2024), which could also be obscured along our line of sight or faded away, leaving a fossil ionized nebula, as seen in *voorwerpen* (Lintott et al. 2009; Keel et al. 2015; Finlez et al. 2022; Venturi et al. 2023; Solimano et al. 2025). Investigating the physical properties of these extended gas nebulae and relating their presence and properties to the SFH of their central galaxies may hold the key to understanding how SMBHs quench galaxies (Nelson et al. 2019). In turn, this may reveal how massive, quiescent galaxies seemingly appear out of nowhere.

In this article, we report the discovery of a candidate 'blowout' system at redshift $z = 6$. This galaxy, JADES-GS-518794, is found at the centre of a large overdensity of galaxies, and is surrounded by a remarkably extended and luminous emission-line nebula. After presenting the data (Section 2), we describe the redshift determination of the system (Section 3) and the morphology of the central galaxy (Section 4). Section 5 presents the spectral energy distribution (SED) of the main components of the system, while the energetics of the emission-line regions are discussed in Section 7. In Section 8, we investigate the large-scale environment, before proceeding to interpret our findings and discuss their implications (Section 9). A short summary is provided in Section 10.

Throughout this work, we assume the Planck Collaboration VI (2020) Lambda cold dark matter (ΛCDM) cosmology, where we calculate a physical scale of 5.89 kpc arcsec^{-1} at redshift $z = 5.89$. Unless otherwise specified, physical scales are given as proper quantities. All stellar masses are total stellar mass formed, assuming a Chabrier (2003) initial mass function, integrated between 0.1 and 120 $M_\odot$. All magnitudes are in the AB system (Oke & Gunn 1983) and all EWs are in the rest frame, with negative EW corresponding to line emission.

2 DATA

Our target galaxy JADES-GS-518794 (Fig. 1) is a red, faint galaxy ($F_{F444W} = 0.75 \pm 0.01$ μJy, 24.2 mag[1]) at RA 53.00804, Dec. −27.85477, located in the GOODS South (GOODS-S) cosmological field (Great Observatories Origins Deep Survey; Giavalisco et al. 2004). The source was first detected by the *Spitzer* IRAC/MUSYC Public Legacy Survey in the Extended CDF-South (SIMPLE; Damen et al. 2011) in IRAC ch1 and ch2 (SIMPLE ID 26553; RA 53.007931, Dec.−27.854734; separation 0.4 arcsec).The IRAC ch2 (4.5 μm) flux is $F_{ch2} = 1.7 \pm 0.2$ μJy, higher than the *JWST* value by a factor of two. This flux mismatch and the centroid offset are possibly due to source confusion between the galaxy, the surrounding nebula, and nearby foreground galaxies. This is exacerbated by the much larger point spread function (PSF) of IRAC ch2 versus NIRCam *F*444*W* (full width at half-maximum, FWHM = 1.9 arcsec; Damen et al. 2011 versus 0.14 arcsec; Ji et al. 2024b). No detection at redder wavelengths is reported, so from here on we focus on the new data from *JWST*. Our NIRCam observations come from the Guaranteed Time Observations (JADES, *JWST* Advanced Deep

[1]We used a Kron aperture, determined as described in Rieke et al. (2023). This may incur in contamination from diffuse H α, but the flux from modelling the light profile in *F*410*M* (where no contamination from diffuse nebular emission is present) is comparable, at $F_{F410M} = 0.67 \pm 0.01$ μJy or 24.3 mag (see Section 4).

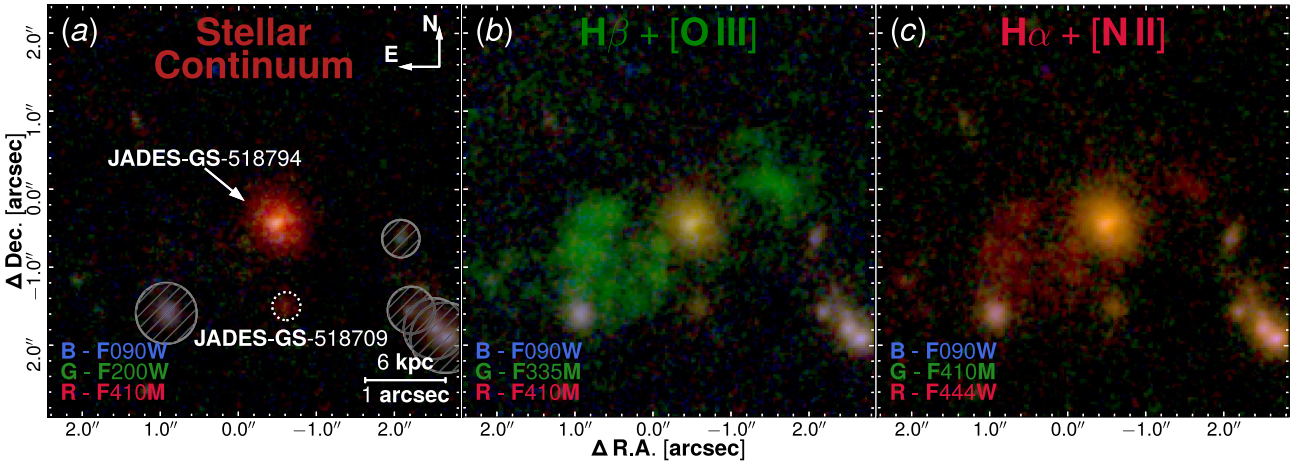

Figure 1. *JWST*/NIRCAM false-colour images of JADES-GS-518794, highlighting continuum emission (panel a), H β and [O III]$\lambda\lambda$4959, 5007 (captured by *F*335*M*; panel b), and H α and [N II]$\lambda\lambda$6548, 6583 (falling in *F*444*W*; panel c). Hatched sources in panel (a) are foreground galaxies (identified via conspicuous flux blueward of the Ly α break at $z = 5.89$, detected by *HST*/ACS). The galaxy JADES-GS-518794 is located at the centre of a 25-kpc diameter nebula, extending on both sides and displaying arc-like shapes, reminiscent of shock fronts/hot gas bubbles. A possible quiescent satellite is also present (JADES-GS-518709, dotted circle in panel a, also visible in panels b and c).

Table 1. Summary of the new NIRCam observations (PID 1286, Obs 6) used to find and study JADES-GS-518794. An in-depth presentation of data from PID 1286 will be presented in JADES Collaboration (in preparation).

Filter name	t_{exp} (ks)	Filter name	t_{exp} (ks)
*F*070*W*	5.67	*F*277*W*	8.50
*F*090*W*	11.34	*F*335*M*	5.67
*F*115*W*	11.34	*F*356*W*	5.67
*F*150*W*	8.50	*F*410*M*	11.34
*F*200*W*	5.67	*F*444*W*	11.34

Extragalactic Survey; Eisenstein et al. 2023a), obtained as part of programme ID (PID) 1286 (PI N. Lützgendorf), and consists of 5.67–11.34 ks integrations using various wide- and medium-band filters, as detailed in Table 1. We supplement the JADES NIRCam observations with legacy *Hubble Space Telescope* (*HST*)/ACS imaging at shorter wavelengths from the Hubble Legacy Field data (Whitaker et al. 2019). The NIRCam data reduction follows the approach presented in Rieke et al. (2023), Eisenstein et al. (2023b), Robertson et al. (2024), and D'Eugenio et al. (2025a). Improvements with respect to the procedures highlighted in these papers will be presented in a future data-release article (JADES Collaboration, in preparation).

For the main galaxy JADES-GS-518794, we also use mid-infrared (MIR) photometry from *Spitzer*/IRAC and MIPS and from *JWST*/MIRI.For *Spitzer*, we retrieve images from the Rainbow data base obtained with IRAC ch3 and ch4 (5.8 and 8 μm; Pérez-González et al. 2008; Guo et al. 2012) and with MIPS 24 μm (Pérez-González et al. 2005). Since the source is detected at most tentatively, we use photometry extracted from circular apertures centred on the nominal position of the target. For IRAC ch3 we use apertures of 1.5- and 2-arcsec radius, which give the same flux of 24.5 ± 0.5 mag (after applying aperture corrections for point like sources). For the noisier ch4, we use a smaller 0.75-arcsec aperture to derive an upper limit of 23.2 mag. Similarly, we find only an upper limit in MIPS 24 μm. For MIRI, we use data from PID 1180, which was not previously reduced due to a guide-star failure. However, the observations in *F*1500*W* show a clear detection at the location of JADES-GS-518794.

Photometric redshifts z_{phot} were obtained using EAZY (Brammer, van Dokkum & Coppi 2008), using photometry from JADES DR3 (D'Eugenio et al. 2025a) and the procedure described in Hainline et al. (2024). Throughout this paper, we adopt the `z_a` EAZY photometric redshifts described in Hainline et al. (2024), and the uncertainties are defined as (`u68-l68`)/2. For the new region of JADES where JADES-GS-518794 lies, these measurements will be released in the future (Hainline, in preparation).

When characterizing the large-scale environment, photometric redshifts are complemented by slit spectroscopy from the NIRSpec Micro-Shutter Assembly (Ferruit et al. 2022; Jakobsen et al. 2022; obtained by JADES Eisenstein et al. 2023a) and by slitless spectroscopy obtained as part of the programmes: FRESCO (First Reionization Epoch Spectroscopic COmplete Survey; PID 1895; Oesch et al. 2023), SAPPHIRES (Slitless Areal Pure Parallel HIgh-Redshift Emission Survey; PID 6434, PI E. Egami), and PID 4540 (JADES; PI D. Eisenstein).

NIRCam wide-field slitless spectroscopy (WFSS) of JADES-GS-518794 was serendipitously obtained through SAPPHIRES. The row-direction grism (Grism-R) observation was obtained with their observation number 41 through the *F*444*W* filter (3.9–5.0 μm) with a total onsource integration time of 11.8 h. Detailed observation description will be presented by a paper through the SAPPHIRES collaboration (Sun et al. 2025).

3 REDSHIFT DETERMINATION

Both JADES-GS-518794 and the extended region surrounding it (Fig. 1) display clear photometric excess in *F*335*M* relative to *F*356*W*, and in *F*444*W* relative to *F*410*M*. The magnitude of these differences leaves no doubt about their interpretation as emission lines with high EW. At the same time, the galaxy is a clear *F*070*W* dropout and very faint in *F*090*W*, suggesting a redshift around $z \sim 6$. Around this redshift, H β and [O III]$\lambda\lambda$4959, 5007 emission would fall in *F*335*M*, while H α would fall in *F*444*W*, redward of *F*410*M*. The estimated photometric redshift of JADES-GS-518794 is $z_{phot} = 6.03^{+0.16}_{-0.15}$. The extended region surrounding the galaxy consists of two main regions (hereafter: East and West clouds; Fig. 1 b and c). The standard JADES imaging pipeline deblends these two clouds into 10 sources. Of these, eight are consistent with the photometric redshift of JADES-GS-518794, while the two

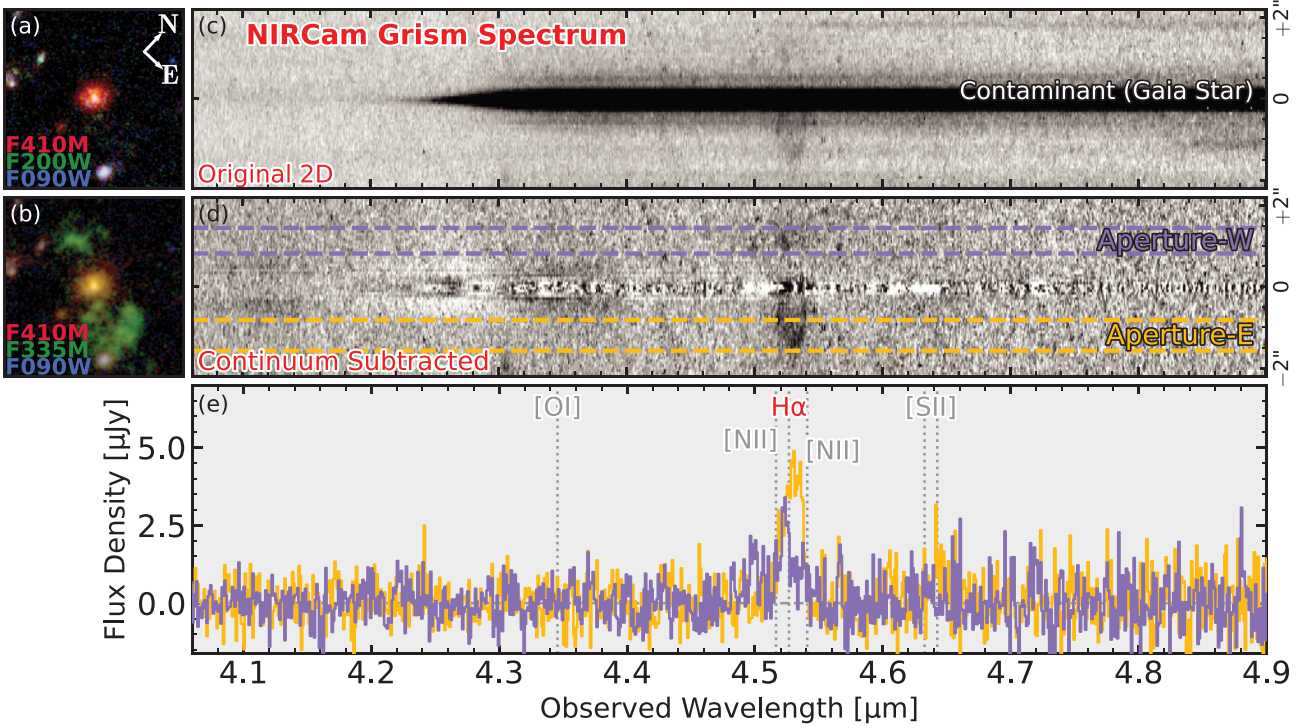

Figure 2. NIRCam *F444W* grism spectrum of JADES-GS-518794 obtained through Cycle-3 PID 6434 (SAPPHIRES). Panels (a) and (b) are the same false-colour RGB images as in Fig. 1(a) and (b), highlighting respectively the stellar continuum and [O III] line emission; the images have been rotated and flipped to align them with the dispersion direction of the 2D grism spectrum, shown on the right. Panels (c) shows the 2D grism spectrum; the bright continuum is from a contaminating *Gaia* star. Panel (d) shows the 2D grism spectrum with the continuum subtracted; two boxcar apertures (W/E) for spectral extraction are shown in pink and yellow, respectively, capturing emission from the East and West clouds (see Fig. 4). Panel (e) shows the 1D grism spectra extracted with the two apertures; for both spectra, we identify the line at ∼4.52 μm as Hα. Other notable emission lines are indicated by vertical dotted lines (grey labels are non-detections).

brightest regions are placed by EAZY at $z_{\rm phot} = 0.01$, with a secondary χ^2 minimum at $z_{\rm phot} \sim 6$. This redshift mismatch is likely due to the fact that the photometry for these sub-regions is dominated by ionized gas emission, with very little underlying galaxy light, and EAZY cannot reproduce the observed colours with galaxy templates. Indeed, when performing SED modelling, we infer extremely high EWs, which we discuss further in Section 5. In any case, these two regions at $z_{\rm phot} = 0.01$ are not detected by *HST*, and their minimum χ^2 value is unsatisfactorily large ($\chi^2 = 140$ and 160). Other nearby objects detected by *HST* are clear foreground galaxies. These have distinctively bluer colour, no photometric excess in the NIRCam filters reported above, and reliable $z_{\rm phot}$ placing them at various redshifts between 1.5 and 3. These foreground galaxies are marked by hatched circles in Fig. 1(a).

We determine the spectroscopic redshift of JADES-GS-518794 through NIRCam WFSS. The SAPPHIRES grism spectra were processed through the routine outlined by Sun et al. (2023), and the codes and calibration data are publicly available.[2] We refer interested readers to the SAPPHIRES early data release article for updated descriptions of NIRCam WFSS calibration and SAPPHIRES data processing (Sun et al. 2025).

Fig. 2 displays the reduced *F444W* grism spectrum of our target, which covers the spectral region including Hα, [N II]$\lambda\lambda$6548, 6583 and [S II]$\lambda\lambda$6716, 6731. JADES-GS-518794's spectrum is severely contaminated by the spectrum of the bright *Gaia* star (Gaia DR3 5057502837774749952), which hampers measuring the central galaxy's redshift. However, diffuse line emission is visible at ~ 4.52 μm, which is spatially offset from the bright continuum contaminant. We interpret the emission as Hα emission at $z \sim 5.89$ according to the JADES $z_{\rm phot}$. The diffuse Hα emission is spatially aligned with two line-emitting regions identified in NIRCam imaging data, which are to the west and east of the central galaxy (Fig. 1). We therefore extract the spectra for the two regions using boxcar apertures, and the heights are 0.57 and 0.69 arcsec for aperture-W and -E, respectively. The continuum is modelled and subtracted through smoothing spline interpolation with line-emitting wavelength (4.49–4.55 μm) masked. We fit the emission lines with a Gaussian profile in the continuum-subtracted 1D spectra. After considering the spatial offsets of the line-emitting region relative to the central galaxy in both NIRCam image and spectra, we measure spectroscopic redshifts of 5.903 and 5.884 for the West and East clouds, respectively. The redshift uncertainty is estimated to be $\Delta z = 0.002$, which is dominated by the uncertainty of centroid determination in both imaging and grism data. The redshift offset between the two clouds corresponds to a velocity offset of 830 ± 130 km s^{-1}. The spectrum of the East clouds appears dominated by Hα emission, with no evidence for [N II]$\lambda\lambda$6548, 6583 or [S II]$\lambda\lambda$6716, 6731. The spectrum of the West cloud displays a secondary emission-line peak near the wavelength of [N IIλ6583], reaching 30 per cent of the Hα peak. However, this emission could also be due to Hα, spectrally offset with respect to the main peak due to the spatially extended nature of the cloud and to the grism degeneracy between spatial offset and spectral shift. Given this 30 per cent upper limit

[2] https://github.com/fengwusun/nircam_grism/

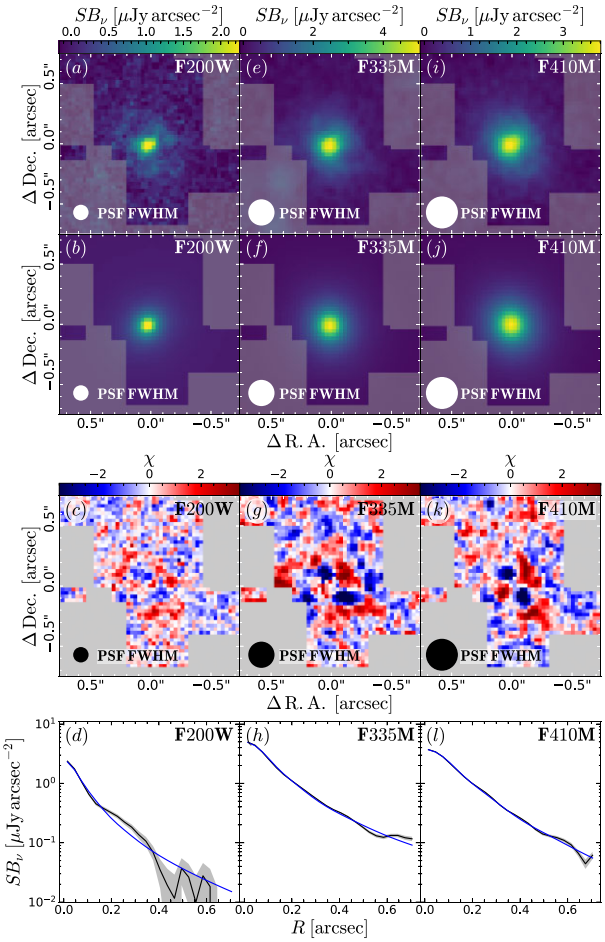

Figure 3. Morphological analysis of JADES-GS-518794, with each column showing the results for a different NIRCam filter as indicated. From top to bottom, the rows are the data, fiducial Sérsic model, χ residuals, and radial surface-brightness profile. The grey rectangles mask nearby sources that are not included in the fit.

and the fainter nature of the West cloud, we can safely conclude that at wavelengths around 4.5 μm, the emission is dominated by Hα.

4 MORPHOLOGICAL PARAMETERS

We use PYSERSIC (Pasha & Miller 2023) to measure the structural parameters of JADES-GS-518794, using a single Sérsic light profile. We limit our models to *F*200*W*, capturing the rest frame near-ultraviolet (UV) blueward of the Balmer break, *F*335*M* (tracing Hβ and [O III] emission), and *F*410*M*, tracing the stellar continuum in the rest-frame optical. In each band, we use empirical PSFs measured from the JADES data (Ji et al. 2024b). Nearby and foreground sources are masked (Fig. 3). The fiducial model is the maximum a posteriori model with a Student's t loss function, while the marginalized posterior probabilities on the free parameters are estimated using the stochastic variational inference method (Hoffman, Blei & Paisley 2013).

A summary of the analysis is presented in Fig 3; the marginalized posterior probabilities of the model parameters are reported in Table 2. In all bands, the model prefers a Sérsic index of 2–3, particularly at the bluest wavelengths. The half-light semimajor axes span 0.21–0.29 arcsec, corresponding to 1.2–1.7 kpc, which is typical

Table 2. Morphological parameters of the central galaxy JADES-GS-518794 with PYSERSIC.

Filter	Flux (μJy)	R_e (arcsec)	Sérsic n –
*F*200*W*	0.19 ± 0.02	0.21 ± 0.03	2.8 ± 0.3
*F*335*M*	0.91 ± 0.02	0.29 ± 0.02	3.1 ± 0.1
*F*410*M*	0.65 ± 0.01	0.22 ± 0.01	2.1 ± 0.1

for star-forming galaxies at this redshift (Ormerod et al. 2024), but much larger than quiescent galaxies (by extrapolating measurements at $z \lesssim 5$; Ji et al. 2024a, or via direct measurements at $z = 7.3$; Weibel et al. 2025). The galaxy images and Sérsic index reaching $n = 3$ suggest the presence of a compact core surrounded by more diffuse emission on galaxy scales, but modelling the galaxy with an additional point source is disfavoured, with the fiducial point source flux statistically consistent with 0.

Inspecting the fit residuals, we find evidence of substructures not captured by a single Sérsic profile. These substructures appear as regions where the residuals have consistently positive residuals (particularly evident in *F*200*W* in panel c). In addition, in *F*200*W*, the presence of substructures is also evident in the excess of the observed surface-brightness profile relative to the best-fitting model (black versus blue lines in panel d). These residual structures appear aligned almost orthogonally to the position angle we infer from the regions with the highest surface brightness. Due to their irregular structures, these residuals suggest some recent merger event, rather than a dynamically relaxed component.

5 SED MODELLING

We model the SED of each source using PROSPECTOR (Johnson et al. 2021), following the set-up of Tacchella et al. (2022, hereafter T22). The redshift is free, but we adopt a Gaussian prior with mean $z = 5.89$ and dispersion $\sigma = 0.01$. Preliminarily, we tested a Gaussian prior with mean $z = z_{\rm phot}$ and dispersion $\sigma = 0.5$, and verified that the resulting posterior probability is statistically consistent with the spectroscopic redshift. We use flat priors on both stellar mass $M_\star$ and metallicity $Z_\star$ (in log space). We test different SFH parametrizations, but as a fiducial model we use a piecewise constant SFH over 10 time bins (using six time bins gives statistically consistent results). The first three bins are chosen between $t = 0$–10, 10–30, and 30–100 Myr, with t being the look-back time from the epoch of observation. The remaining seven bins are logarithmically spaced between $t = 100$ and $t = 730$ Myr, the look-back time between $z = 5.89$ and $z = 20$. The SFR is set to 0 at any epoch earlier than $z = 20$. In addition to the total mass formed, this parametrization includes nine free parameters, which are taken to be the logarithm of the SFR ratio between adjacent time bins. We adopt a probability prior that favours a rising SFR with time, mirroring the increasing accretion rate of dark matter haloes with cosmic time (e.g. Wechsler et al. 2002; Neistein & Dekel 2008; Dekel et al. 2013; Tacchella et al. 2018). We use the implementation presented in Turner et al. (2025) for the massive quiescent galaxy ZF-UDS-7329 (Glazebrook et al. 2024). Remarkably, this prior yields a better agreement between the SFH inferred from the $z \sim 3$ observations and direct measurements of the SFR of galaxies at earlier epochs (Turner et al. 2025). The prior is enforced by a Student's t probability distribution on the logarithm of the ratio of the SFRs between adjacent time bins, with a redshift-dependent mean for each time bin (equation 4 in Turner et al. 2025) and with a generous scale parameter of 1, which

Table 3. Summary of the model parameters, prior and posterior probabilities for the central galaxy JADES-GS-518794 from PROSPECTOR.

Parameter (1)	Description (2)	Prior (3)	Fiducial (4)	Continuity (5)	Bursty (6)
$z_{\rm obs}$	Redshift	$\mathcal{N}(z_{\rm spec}, 0.01)$	$5.89^{+0.01}_{-0.01}$	$5.89^{+0.01}_{-0.01}$	$5.89^{+0.01}_{-0.01}$
$\log M_\star(\mathrm{M}_\odot)$	Total stellar mass formed	$\mathcal{U}(6, 13)$	$10.1^{+0.1}_{-0.2}$	$10.2^{+0.1}_{-0.1}$	$10.1^{+0.1}_{-0.1}$
$\log Z(\mathrm{Z}_\odot)$	Stellar metallicity	$\mathcal{U}(-2, 0.19)$	$-0.7^{+0.6}_{-0.5}$	$-0.7^{+0.6}_{-0.6}$	$-0.5^{+0.5}_{-0.5}$
log SFR ratios	Ratio of the log SFR between adjacent bins of the non-parametric SFH	$\mathcal{T}(\Xi_i, 1, 2)^a$	–	–	–
n	Power-law modifier of the dust curve (T22, their equation 5)	$\mathcal{U}(-1.0, 0.2)$	$-0.0^{+0.2}_{-0.2}$	$-0.1^{+0.2}_{-0.2}$	$-0.2^{+0.3}_{-0.3}$
τ_V	Optical depth of the diffuse dust (T22, their equation 5)	$\mathcal{G}(0.3, 1; 0, 2)$	$0.5^{+0.2}_{-0.2}$	$0.5^{+0.2}_{-0.2}$	$0.3^{+0.2}_{-0.1}$
μ	Ratio between the optical depth of birth clouds and τ_V (T22, their equation 4)	$\mathcal{G}(1, 0.3; 0, 2)$	$1.0^{+0.4}_{-0.4}$	$1.0^{+0.3}_{-0.3}$	$1.0^{+0.4}_{-0.3}$
$\log Z_{\rm gas}(\mathrm{Z}_\odot)$	Metallicity of the star-forming gas	$\mathcal{U}(-2, 0.19)$	$0.0^{+0.2}_{-0.3}$	$0.0^{+0.2}_{-0.4}$	$0.0^{+0.2}_{-0.3}$
$\log U$	Ionization parameter of the star-forming gas	$\mathcal{U}(-4, -1)$	$-2.0^{+0.8}_{-0.8}$	$-2.3^{+0.8}_{-0.7}$	$-2.4^{+0.8}_{-0.6}$
$\log \mathrm{SFR}_{10}(\mathrm{M}_\odot\ \mathrm{yr}^{-1})$	Star formation rate averaged over the last 10 Myr	–	$1.4^{+0.2}_{-0.4}$	$1.3^{+0.2}_{-0.3}$	$1.3^{+0.2}_{-0.4}$
$\log \mathrm{SFR}_{100}(\mathrm{M}_\odot\ \mathrm{yr}^{-1})$	Star formation rate averaged over the last 100 Myr	–	$1.2^{+0.4}_{-0.5}$	$1.2^{+0.2}_{-0.3}$	$1.1^{+0.4}_{-0.3}$
age (Gyr)	Mass-weighted stellar age	–	$0.23^{+0.7}_{-0.6}$	$0.40^{+0.09}_{-0.08}$	$0.38^{+0.10}_{-0.10}$
EW([O II]) (Å)	Equivalent width of [O II]λλ3726, 3729	–	-30^{+20}_{-40}	-40^{+20}_{-60}	-40^{+25}_{-60}
EW(Hβ+[O III])(Å)	Equivalent width of H β and [O III]λλ4959, 5007	–	-130^{+80}_{-90}	-140^{+60}_{-70}	-130^{+70}_{-90}
EW(Hα+[N II]) (Å)	Equivalent width of H α and [N II]λλ6548, 6583	–	-310^{+170}_{-170}	-330^{+130}_{-140}	-320^{+150}_{-190}
D(Balmer)	Balmer-break index of Binggeli et al. (2019)	–	$2.24^{+0.16}_{-0.18}$	$2.25^{+0.15}_{-0.13}$	$2.27^{+0.15}_{-0.20}$
D_n4000	4000 Å break index of Balogh et al. (1999)	–	$1.14^{+0.03}_{-0.03}$	$1.15^{+0.03}_{-0.02}$	$1.17^{+0.02}_{-0.03}$
$z_{\rm obs}$	Redshift (alternative run)	$\mathcal{N}(z_{\rm phot}, 0.5)^b$	$5.8^{+0.2}_{-0.1}$	$5.9^{+0.1}_{-0.1}$	$5.9^{+0.1}_{-0.1}$

Note. (1) Parameter name (and units where applicable), (2) parameter description, (3) parameter prior probability distribution; $\mathcal{N}(\mu, \sigma)$ is the normal distribution with mean μ and dispersion σ; $\mathcal{U}(a, b)$ is the uniform distribution between a and b; $\mathcal{T}(\mu, \sigma, \nu)$ is the Student's t distribution with mean μ, dispersion σ and ν degrees of freedom; $\mathcal{G}(\mu, \sigma, a, b)$ is the normal distribution with mean μ and dispersion σ, truncated between a and b, (4) median and 16th–84th percentile range of the marginalized posterior distribution for the model with the fiducial SFH prior (rising SFH); the nine log SFR ratios are considered nuisance parameters so we do not report their posterior statistics, (5) same as (4), but for the model with the 'continuity' SFH prior, (6) same as (4), but for the model with the 'bursty' SFH prior. [a] The fiducial model uses a rising SFH prior (Turner et al. 2025); for each time bin i in the SFH, the mean of the log SFR ratio Ξ_i is set by the accretion rate of dark matter haloes (Turner et al. 2025, their equation 4). For the continuity and bursty SFH priors, $\Xi_i = 0$; for the continuity prior only, the scale parameter of the Student's t prior is set to 0.3. [b] This row shows the posterior redshift probability from alternative runs of PROSPECTOR where the only difference is the prior probability on the redshift; in this run, we assumed as prior $z_{\rm phot}$. All the resulting posterior probabilities are statistically consistent with the spectroscopic redshift.

allows >1 dex variations in SFR. We use a variable dust-attenuation law, parametrized as a free power-law modification index n with respect to the Calzetti curve (Calzetti et al. 2000; Noll et al. 2009). This dust-attenuation index is tied to the strength of the UV bump, following the empirical relation by Kriek & Conroy (2013). The overall attenuation is parametrized by the V-band equivalent optical depth τ_V, with an additional power-law attenuation screen towards birth clouds (Charlot & Fall 2000), assumed to fully enshroud all stars younger than 10 Myr. We use the Madau (1995) intergalactic medium absorption profile. Stars with ages younger than 10 Myr are associated with nebular emission, which is parametrized by the ionization parameter U and by the gas metallicity $Z_{\rm gas}$. For each guess of these two model parameters, the strength of the nebular emission is obtained from pre-computed CLOUDY models (Ferland et al. 2017), using the set-up presented in Byler et al. (2017). Each parameter is assigned a prior with varying degrees of information, which we summarize in Table 3. By adopting this complex model, we do not claim nor hope to meaningfully constrain all 17 free parameters, particularly given that a fit to nine photometric data points alone cannot break the degeneracy between stellar age, metallicity, and dust attenuation (Trager et al. 1998). However, this set-up enables us to obtain realistic uncertainties and degeneracies in the most relevant parameters we are interested in: $M_\star$ and recent trends in the SFR.

5.1 Central galaxy

The marginalized posterior probabilities of the model parameters for JADES-GS-518794 are reported in Table 3. When using as input the photometric redshift from EAZY, the posterior probability on the PROSPECTOR redshift is fully consistent with the spectroscopic redshift of the extended nebula (Section 3). Therefore, to reduce the uncertainties, we use as default the much narrower probability prior from SAPPHIRES. In this case, the prior is more informative than the photometry, so the posterior is identical to the prior probability.

The observed SED and fiducial model are in Fig. 4(b), with the fit residuals in panel (c). The galaxy SED displays a relatively strong Balmer break [D(Balmer) $= 2.24^{+0.16}_{-0.18}$; using the definition of Binggeli et al. 2019], with a mass-weighted stellar age of 230 ± 70 Myr, intermediate between recently quenched galaxies (e.g. JADES-GS-z7-01-QU; Strait et al. 2023; Looser et al. 2024b; Baker et al. 2025b) and quiescent galaxies (like RUBIES-UDS-QG-z7; Weibel et al. 2025). The stellar mass is of order $M_\star = 10^{10}\ \mathrm{M}_\odot$, similar to that of RUBIES-UDS-QG-z7 and much larger than JADES-GS-z7-01-QU.

The SFH (Fig. 4d) displays a rapid rise at early times, but this is driven entirely by the adopted prior. At later times the SFR declines (in the last 100–10 Myr), followed by an upturn in the most recent

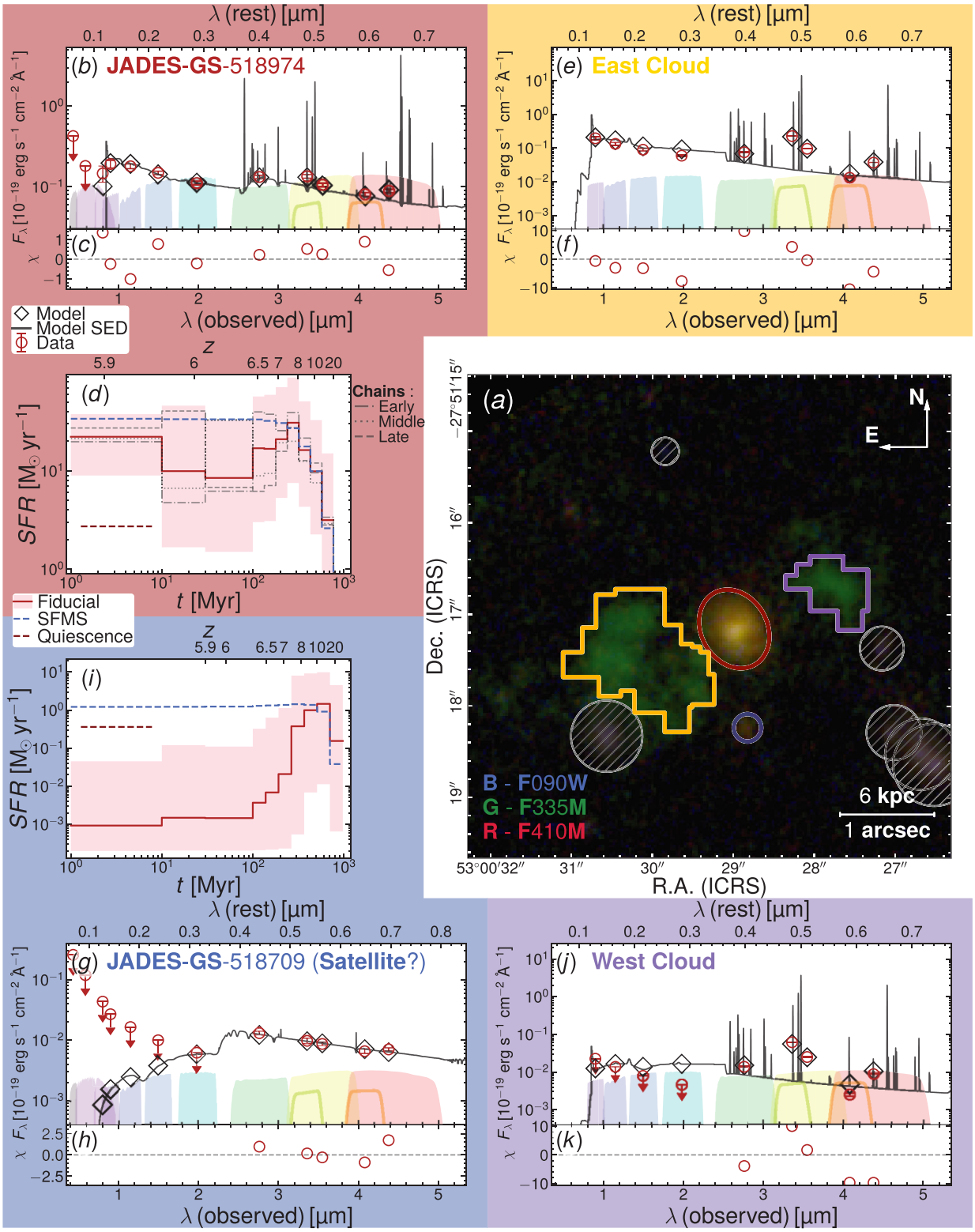

Figure 4. Apertures (panel a) and PROSPECTOR SED models (panels b–k). Observed SEDs (red circles) and fiducial models (black diamonds) are accompanied by the model SED (black line) and residuals χ (adjacent bottom panels). The *HST*/ACS and *JWST*/NIRCam filters are highlighted by the shaded regions, while thick solid lines are NIRCam medium-band filters. For the main target JADES-GS-518794 and the candidate satellite we also show the SFH [panels d and i, with the star-forming main sequence of Popesso et al. (2023) shown by the blue dashed line]. These two galaxies display a clear break at 2.5 μm, corresponding to a Balmer break at $z \approx 6$. Both SFHs display the early rise due to the prior; the satellite then quenches at $z = 7$–8 and becomes quiescent. JADES-GS-518794 also displays a downturn in SFR around 10–100 Myr before observation, while a recent upturn in the last 10 Myr could be due to the photometric excess, consistent with both a resurrection of the SFR or strong AGN. The downturn in SFR is robust and driven by the observed Balmer break; the large uncertainties about the SFR in the range 10–100 Myr reflect the inability of the data to distinguish scenarios of early versus late downturn (see median of individual chains in grey). The line-emitting clouds (panels e–f and j–k) are poorly fit by PROSPECTOR, supporting their interpretation as gas clouds and not tidally disrupted satellites.

10 Myr. The inference of this downturn is driven by the large flux difference between *F*200*W* and *F*277*W*, the bands bracketing the Balmer break. PROSPECTOR considers the flux excess of *F*277*W* with respect to *F*200*W* to be too large to be due to emission lines (e.g. [O II]λλ3726, 3729, [Ne III]λλ3869, 3967), and fits this excess as a stellar Balmer break (Fig. 4b). Indeed, among the 130 000 models explored by prospector during the inference, the model with the strongest [O II]λλ3726, 3729 emission (EW([O II]) = −272 Å) still requires a noticeable Balmer break D(Balmer) = 1.99. Besides this relatively high value, this particular SED model is highly disfavoured by the data, with a difference in log evidence of 11 relative to the maximum a posteriori model. We can also rule out strong dust attenuation causing the flux drop between *F*277*W* and *F*200*W*, because the continuum appears to be rather blue in the rest-frame UV. Notice that the model prefers a Balmer break despite the rising SFH prior, which favours high SFR at recent times and hence is biased against a Balmer break. Rare scenarios like strong shocks could power extremely bright [O II]λλ3726, 3729 emission (Helton et al. 2021), but these cases are extremely rare around non-quasar galaxies (D'Eugenio et al. 2025b).

The scatter about the fiducial SFH is particularly large in the time window between 10 and 100 Myr prior to observation, calling into question the robustness of the claimed downturn. But this large scatter does not take into account that the SFR values in different time bins are strongly anticorrelated with each other, due to the inability of the data to break the degeneracy between early versus late declines in the SFR. This anticorrelation arises from the fact that any overestimate of the SFR at early times leads to an underestimate at later times, while keeping the strength of the Balmer break approximately the same. To illustrate this point, in Fig. 4(d) we also show the median SFH of all the chains whose SFR peaks earlier than 100 Myr (early, dot–dashed grey line), between 30 and 100 Myr (middle, dotted grey line), and between 10 and 30 Myr (late, dashed line). These three SFHs underscore that there are no acceptable solutions where the galaxy kept forming stars at a constant rate throughout the period 10–100 Myr; after all, this would not be consistent with the Balmer break. Hence the inferred downturn in SFR is robust, even though with photometry alone we cannot time this event precisely.

At more recent times $t < 10$ Myr, there is a recent upturn in SFR which is needed to explain the flux excess in *F*335*M* and *F*444*W* with respect to *F*356*W* and *F*410*M*, respectively. This photometric excess is interpreted by PROSPECTOR as being due to recent star formation, causing bright Hβ and [O III]λλ4959, 5007 in *F*335*M* and Hα in *F*444*W*. However, this strong line excess could also be caused by a type-1 AGN, hence the recent 10-Myr upturn in SFR cannot be tested without spectroscopy.

To understand the robustness of these results against the adopted SFH prior, we also considered the 'continuity' prior, with the same time bins as the fiducial model, but with the prior probability on the log SFR ratios centred at 0 with a scale of 0.3 (Leja et al. 2019); and the 'bursty' prior, same as the continuity prior but with a scale of 1 (Tacchella et al. 2022). The 'continuity' and 'bursty' priors implicitly assume a constant SFH across all of the time bins. The model inference with either of these priors yields consistent redshifts, stellar mass, and recent shape of the SFH. The major difference is in the mass-weighted stellar age, where the rising SFH prior results in younger age (Table 3) by suppressing the earliest stages of star formation (yet the age difference between the fiducial and alternative models is not statistically significant, only 1.5σ).

5.2 A low mass associated satellite?

In the mass maps traced by *F*410*M* (rest frame 6000 Å; Fig. 1a), the only other source in the vicinity of JADES-GS-518794 is the faint galaxy JADES-GS-518709, located 1 arcsec (5.89 kpc) to the South of the main galaxy. The photometric redshift of this source is uncertain (the EAZY fit to the source is $z_{\rm phot} = 4.8^{+0.6}_{-0.4}$) owing to the faint photometry of the source in the *HST*/ACS and NIRCam filters shortward of 2.0 μm (Fig. 4g). We do observe a clear drop between the *F*277*W* and *F*200*W* filters which is consistent with a strong Balmer break at the redshift $z = 5.89$ of JADES-GS-518794. Newer observations in *F*200*W* also reveal a clear detection in *F*200*W* (9σ), which rules out the *F*277*W* break being a Lyα break.[3] Interpreting the photometric drop as a Balmer break would be in agreement with the relatively flat *F*335*M* to *F*356*W* and *F*444*W* to *F*410*M* colours, which imply a lack of [O III]λλ4959, 5007 and Hα emission at this redshift. Ironically, we cannot confirm if this galaxy is a faithful satellite of JADES-GS-518794 or not, given the EAZY preference for a lower redshift which is primarily driven by the observed *F*090*W*–*F*115*W* colour for the source. Still, the spatial proximity and possible Balmer break compel us to explore the scenario of a post-starburst satellite. For this purpose, we extract the photometry of JADES-GS-518709 within a circular aperture of radius 0.25 arcsec (CIRC3 in the photometric catalogue, which we represent with a small blue circle in Fig. 4a) and run the PROSPECTOR model inference with the same set-up as JADES-GS-518794. The resulting SED is shown in Fig. 4(g) and the SFH is in panel (i). Using the same prior probability distribution on the redshift as for JADES-GS-518794, the inferred posterior distribution is $z = 5.3 \pm 0.3$, lower but still statistically consistent with the redshift of JADES-GS-518794 as well as the EAZY photometric redshift. Emboldened by this agreement, we repeat the inference using as redshift prior for JADES-GS-518709 the same spectroscopic prior for JADES-GS-518794. The posterior probabilities of the parameters of this fiducial model are reported in Table 4. The mass is $M_\star = 10^{9.3}$ M$_\odot$, six times smaller than JADES-GS-518794. The current and recent SFRs are both undetected, and the general shape of the SFH implies that this galaxy, if confirmed to be at $z = 5.89$, reached the peak of its SFH at $z = 7$–10 (roughly 100 Myr before JADES-GS-518794) and then quenched permanently, reaching a sufficiently low SFR for 100 Myr to be classified as quiescent. Owing to the faint nature and lack of emission lines in JADES-GS-518709, this scenario requires deep spectroscopy to be confirmed.

5.3 Emission-line regions

The large emission-line regions surrounding JADES-GS-518794 are unlikely to be dominated by star formation photoionization, as we will demonstrate in this Section. Galaxies have not been observed to display the combination of very large size and very high [O III]λλ4959, 5007 and Hα EWs seen in the SED of these clouds (Figs 4e and j). Large emission-line region sizes are associated with high $M_\star$ (Shen et al. 2003; van der Wel et al. 2014; Ito et al. 2024; Ji et al. 2024a; Ormerod et al. 2024; Martorano et al. 2024; Miller et al. 2025; Ward et al. 2024), while high EWs are associated with young, low-mass galaxies.

[3]For consistency with the rest of the article, the SED fitting uses the v0.9.5 photometry, where *F*200*W* is not detected. Updating to the deeper photometry gives a younger SFH, but confirms a strong Balmer break.

Table 4. Summary of the posterior probabilities for the PROSPECTOR model parameters of the candidate quiescent satellite JADES-GS-518709 and for the East and West clouds.

Parameter [a]	JADES-GS-518709	East cloud[b]	West cloud[b]
$\log M_\star(\mathrm{M}_\odot)$	$9.3^{+0.1}_{-0.1}$	$8.39^{+0.06}_{-0.04}$	$8.0^{0.3}_{-0.1}$
$\log Z(\mathrm{Z}_\odot)$	$-1.6^{+0.5}_{-0.3}$	$-1.8^{+0.1}_{-0.1}$	$-1.75^{+0.04}_{-0.05}$
n	$-0.7^{+0.4}_{-0.2}$	$-0.98^{+0.06}_{-0.02}$	$-0.9^{+0.7}_{-0.1}$
τ_V	$0.5^{+0.2}_{-0.2}$	$0.14^{+0.01}_{-0.02}$	$0.30^{+0.13}_{-0.06}$
μ	$1.0^{+0.3}_{-0.3}$	$0.2^{+0.6}_{-0.2}$	$0.4^{+0.4}_{-0.3}$
$\log Z_{\mathrm{gas}}(\mathrm{Z}_\odot)$	$-0.9^{+0.9}_{-0.8}$	$-0.70^{+0.01}_{-0.01}$	$-0.69^{+0.02}_{-0.01}$
$\log U$	$-2.8^{+1.1}_{-0.8}$	$-1.2^{+0.1}_{-0.1}$	$-1.04^{+0.03}_{-0.07}$
$\log \mathrm{SFR}_{10}(\mathrm{M}_\odot\ \mathrm{yr}^{-1})$	$-1.0^{+0.8}_{-1.6}$	$1.21^{+0.02}_{-0.01}$	$0.73^{+0.12}_{-0.03}$
$\log \mathrm{SFR}_{100}(\mathrm{M}_\odot\ \mathrm{yr}^{-1})$	$-0.8^{+1.3}_{-1.5}$	$0.35^{+0.05}_{-0.03}$	$-0.20^{+0.19}_{-0.05}$
age (Gyr)	$0.30^{+0.19}_{-0.16}$	$0.04^{+0.01}_{-0.01}$	$0.05^{+0.02}_{-0.01}$
EW([O II]) (Å)	-1^{+1}_{-14}	-230^{+15}_{-18}	-210^{+17}_{-8}
EW(Hβ+[O III]) (Å)	-8^{+7}_{-32}	-7200^{+200}_{-180}	-7000^{+900}_{-450}
EW(Hα+[N II]) (Å)	-30^{+30}_{-150}	-6100^{+180}_{-170}	-5800^{+670}_{-350}
D(Balmer)	$2.7^{+0.4}_{-0.5}$	$1.06^{+0.01}_{-0.01}$	$1.18^{+0.03}_{-0.03}$
$D_{\mathrm{n}}4000$	$1.16^{+0.04}_{-0.04}$	$0.971^{+0.001}_{-0.001}$	$0.992^{+0.005}_{-0.004}$

[a] A description of the parameters and their prior probabilities (where relevant) is in Table 3. [b] We do not interpret the East and West clouds as star-forming galaxies; the parameters of the PROSPECTOR model are reported as a benchmark, and to illustrate that interpreting their emission as a galaxy SED results in implausible parameter combinations. In particular, the extremely small uncertainties on certain parameters (e.g. dust index n, $\log U$, mass-weighted age, $\mathrm{D_n}4000$) are due to the models being a poor match to the observations.

To quantify the plausibility of star formation photoionization, we extract SEDs using large apertures encompassing most of the East and West emission-line regions (yellow and purple lines in Fig. 4a). The resulting models (Table 4) favour low-stellar masses ($10^{8.4}$ and 10^8 $\mathrm{M}_\odot$, respectively for the East and West clouds) with extremely high SFR of 17 and 5 $\mathrm{M}_\odot\ \ \mathrm{yr}^{-1}$. Given their inferred stellar masses and SFR values, these clouds would lie 1.5 and 1.7 dex above the star-forming main sequence (SFMS) at $z = 5.89$ (Popesso et al. 2023). The inferred dust attenuation is also very implausible. The diffuse attenuation (affecting both birth clouds and older stars) is moderate, with $\tau_V = 0.15$ and 0.27, respectively. However, the ratio μ between birth-cloud and foreground attenuation is only 0.3, while typical values are around $\mu = 1$ (Calzetti et al. 2000; Charlot & Fall 2000). The low value of μ arises from the competing requirements of achieving high continuum attenuation, necessary to suppress weak/undetected UV light, while maintaining low emission-line attenuation to preserve the brightness of the emission lines. Similarly, the dust curve is as steep as possible (given the top-hat prior probability cut at $n \geq -1$), because with $n = -1$, the model again attempts to minimize the UV continuum without suppressing the rest-frame optical emission lines.

Nevertheless, even this contrived model cannot fully reproduce the data. For both clouds, the UV continuum is overpredicted by up to 7σ (Figs 4f and k). Moreover, the model clearly overpredicts the optical continuum traced by *F*410*M* (by about 10σ in both cases). Our parametric SFH approach with Student's t probability priors leaves enough flexibility to reproduce sharp bin-to-bin variations in the SFR, because the fat tails on the prior probability are certainly less constraining than the poorly fit 7–10σ Gaussians discussed above. Therefore, these major model mismatches suggest that the star-forming interpretation is either highly incomplete or outright incorrect, with the nebular emission driven by entirely different energy sources.

6 AGN MODELLING

To test for on obscured AGN, we use the SED fitting tool CIGALE (Yang et al. 2022), fitting to the Kron aperture NIRCam photometry to the source. At longer wavelengths, we include ad hoc photometric measurements from both *Spitzer*/IRAC ch3 and ch4 and *JWST*/MIRI (Section 2). These fluxes are important as they help to constrain the possibility of an obscured AGN that may only be visible in the near-to-mid IR. For CIGALE, we employ the SKIRTOR AGN implementation from Stalevski et al. (2016), while the host galaxy stellar-population templates are from Bruzual & Charlot (2003). We used the default SFH, parametrized by a delayed exponential. Dust attenuation assumes the Gordon et al. (2003) law for the AGN, and the Calzetti et al. (2000) law for the stellar populations. The resulting fits are shown in Fig. 5, where we contrast the model where both include and do not include emission from an AGN (panels a and c, respectively). Both models are consistent with the observations within the uncertainties, with reduced χ^2_ν of 1.9 and 1.5 for the model without and with an AGN. However, the AGN model better reproduces the *JWST*/MIRI flux at *F*1500*W*. Overall, the MIR observations are useful to constrain the luminosity of an obscured AGN. The AGN model returns a dust attenuation towards the AGN of $A_V = 4.5 \pm 2.9$ mag. The luminosity is $\log(L_{\mathrm{bol}}\,[\mathrm{erg\ s^{-1}}]) = 45.8 \pm 0.6$ dex, which we treat as an upper limit given the non-detection by *Spitzer*/MIPS at 24 μm and the low reduced χ^2_ν of the non-AGN model. There is a large discrepancy between the data and model around the Balmer-break region, where both CIGALE model fits underpredict the strength of the Balmer break. This is likely due to our SFH set-up in CIGALE, which lacks the flexibility for allowing a period of low SFR followed by a 'crescendo', as we discussed in Section 5.1. Overall, this discrepancy results in a strong disagreement about the recent SFH, with CIGALE inferring that the SFR averaged over the 10 Myr prior to observation is 260 ± 15 $\mathrm{M}_\odot\ \mathrm{yr}^{-1}$. In contrast, the stellar mass is in good agreement with PROSPECTOR, with CIGALE finding $\log(M_\star/\mathrm{M}_\odot) = 10.06 \pm 0.02$, with minimal differences if an AGN is included or not.

7 EMISSION-LINE LUMINOSITY

From the surface brightness distribution of the emission-line regions, we can estimate the flux and equivalent width of the main emission-line groups, H β and [O III]λλ4959, 5007 in *F*335*M* and *F*356*W*, and H α in *F*410*M* and *F*444*W*. For the rest-frame EW of H β and [O III]λλ4959, 5007, since the lines fall in both the medium- and wide-band filters, we use the expression

$$EW(\mathrm{H}\beta + [\mathrm{O\,III}]) \approx \frac{\square_{F335M}}{1+\mathrm{z}} \frac{1 - \frac{1}{\delta_{\mathrm{cont}}} \frac{\lambda^2_{F356W}}{\lambda^2_{F335M}} \frac{F_{\nu\,F335M}}{F_{\nu\,F356W}}}{1 - \frac{\lambda^2_{F356W}}{\lambda^2_{F335M}} \frac{\square_{F335M}}{\square_{F356W}} \frac{F_{\nu\,F335M}}{F_{\nu\,F356W}}} \tag{1}$$

$$\delta_{\mathrm{cont}} \equiv \frac{\lambda^2_{F356W}}{\lambda^2_{F335M}} \frac{F_{\nu\,F335M,\,\mathrm{cont}}}{F_{\nu\,F356W,\,\mathrm{cont}}}, \tag{2}$$

where λ_{F335M} is the pivot wavelength of the *F*335*M* filter, $\square_{F335M}$ is the rectangular width of the *F*335*M* filter (defined as the effective width of the filter divided by its maximum throughput), and δ_{cont} is a continuum-colour correction term, whose value we do not know, due

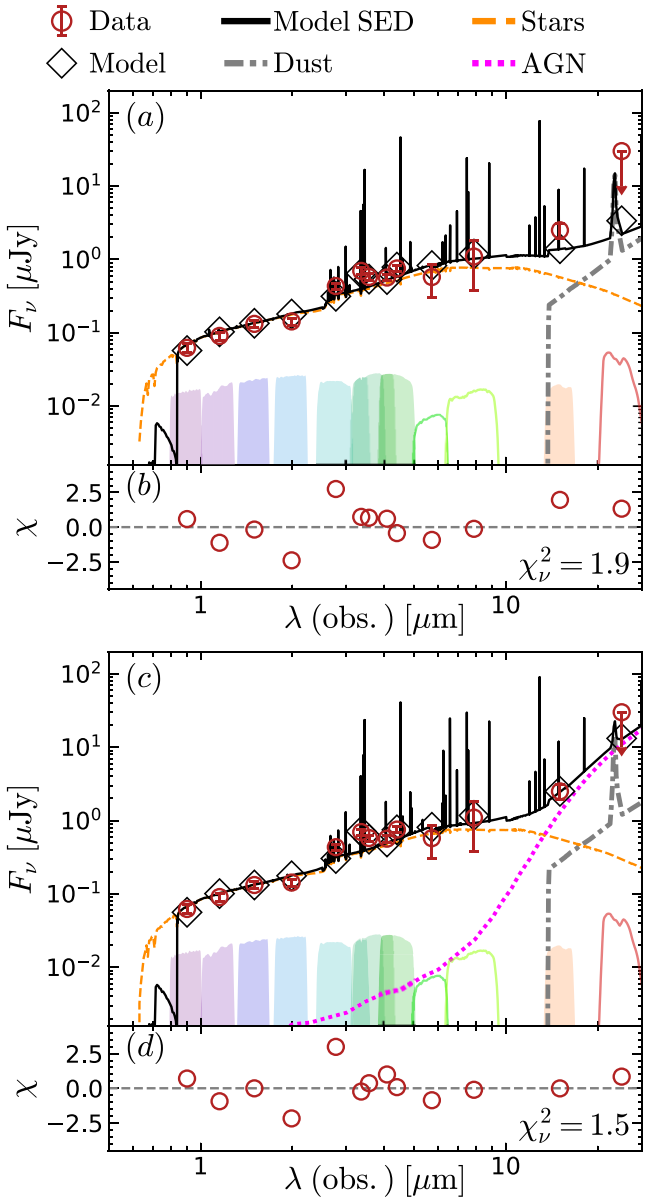

Figure 5. CIGALE SED modelling of the main galaxy JADES-GS-518794, contrasting the model without AGN (panels a and b) and with AGN (panels c and d). The filled filter transmission curves are *JWST*/NIRCam and MIRI filters, while the empty transmission curves are *Spitzer*/IRAC and MIPS. The two models are statistically consistent, as inferred from comparing the reduced χ^2_ν, yet the AGN model is better at reproducing the MIRI $F1500W$ flux, which CIGALE interprets as evidence for an obscured AGN. The MIR data place an upper limit on the AGN luminosity of $L_{\rm bol} \lesssim 10^{45.8}$ erg s^{-1}.

to the lack of sufficient medium bands to characterize the continuum shape (see Appendix A for a derivation). For reference, for a flat continuum in F_λ, $\delta_{\rm cont} \approx 1$. The resulting EW has the same units as $\square_{F335M}$. For Hα, which falls in the wide-band filter but not in the medium-band filter, we have

$$EW({\rm H}\alpha) \approx \frac{\square_{F444W}}{1+z}\left(1 - \delta_{\rm cont}\cdot\frac{\lambda^2_{F410M}}{\lambda^2_{F444W}}\frac{F_{\nu\,F444W}}{F_{\nu\,F410M}}\right) \quad (3)$$

$$\delta_{\rm cont} \equiv \frac{\lambda^2_{F444W}}{\lambda^2_{F410M}}\frac{F_{\nu\,F410M,\,\rm cont}}{F_{\nu\,F444W,\,\rm cont}}. \quad (4)$$

These approximations are somewhat simplistic: because the continuum spectral density features in the denominator of the EW definition, the errors of equations (1) and (3) can be large for any range of EW values. These errors are driven primarily by the colour of the continuum between the two photometric bands used.

In contrast, the corresponding emission-line fluxes are more stable for regions with higher EW values. For Hβ and [O III]$\lambda\lambda$4959, 5007, we have

$$F({\rm H}\beta + [{\rm O\,III}]) \approx 10^{-5}\frac{\rm c}{\lambda^2_{F335M}}\frac{\square_{F335M}\,\square_{F356W}}{\square_{F356W} - \square_{F335M}} \times\left(F_{\nu\,F335M} - \frac{\lambda^2_{F335M}}{\lambda^2_{F356W}}F_{\nu\,F356W}\right), \quad (5)$$

while for Hα we have

$$F({\rm H}\alpha) \approx 10^{-5}\frac{\rm c}{\lambda^2_{F444W}}\square_{F444W} \times\left(F_{\nu\,F444W} - \frac{\lambda^2_{F444W}}{\lambda^2_{F410W}}F_{\nu\,F410M}\right), \quad (6)$$

where the pivot wavelengths and rectangular widths are in units of μm, c is the speed of light in km s^{-1}, F_ν are spectral flux densities in nJy, and the resulting emission-line flux is in units of 10^{-18} erg s^{-1} cm^{-2}. Identical expressions apply to surface brightness, by replacing F_ν with SB_ν.

The surface brightness maps obtained by applying equations (5) and (6) to the JADES data are displayed in Fig. 6. The Hβ + [O III] map (panel a) and Hα map (panel b) reach surface-brightness noise levels of 1.4 and 1.2×10^{-17} erg s^{-1} cm^{-2} arcsec^{-2}, corresponding to 5σ flux sensitivities of 6 and 5×10^{-19} erg s^{-1} cm^{-2} in a circular aperture with 0.15-arcsec radius. The total area where flux is detected in Hβ + [O III] only is 44.6 kpc^2.

To measure total line luminosities, we define two apertures for estimating the emission from the host galaxy and from the nebula. For the host, we define an elliptical aperture with the position angle and shape of the stars in the host galaxy (Section 4), reaching 2 $R_{\rm e}$ (solid line in Fig. 6); for the nebula, we use a much larger circular aperture of radius 2.1 arcsec (dashed line). For the nebula, we measure fluxes of $F({\rm H}\beta + [{\rm O\,III}]) = (163 \pm 2) \times10^{-18}$ erg s^{-1} cm^{-2} and $F({\rm H}\alpha) = (60 \pm 1) \times10^{-18}$ erg s^{-1} cm^{-2}. For comparison, integrating the Hα emission lines from the SAPPHIRES apertures and summing the two clouds we find $F({\rm H}\alpha) = (18 \pm 2) \times10^{-18}$ erg s^{-1} cm^{-2}, implying a flux mismatch of about three. This is not surprising, and may arise from a combination of inaccurate flux measurement from NIRCam photometry, plus low sensitivity of NIRCam/WFSS to diffuse and broad-line emission. Neglecting dust attenuation, the luminosities of the host galaxy in each of the two emission-line groups Hβ + [O III] and Hα are $L_{{\rm H}\beta+[{\rm O\,III}]} = (2.10 \pm 0.04) \times 10^9$ L$_\odot$ and $L_{\rm H\alpha} = (0.86 \pm 0.04) \times 10^9$ L$_\odot$. The nebula (without the host galaxy) has $L_{{\rm H}\beta+[{\rm O\,III}]} = (1.78 \pm 0.02) \times 10^{10}$ L$_\odot$ and $L_{\rm H\alpha} = (0.66 \pm 0.02) \times 10^{10}$ L$_\odot$. In Hβ + [O III], the nebula is 8 times more luminous than the host galaxy. Even in the extreme scenario where the host galaxy is corrected for significant dust attenuation (τ_V $(1 + \mu) \approx 2.7$; Table 3[4]) while assuming no dust for the nebula, the luminosity ratio would still be 0.5, making the nebula comparable to the whole galaxy. To place these measurements in context, we estimate the Hβ luminosity from the Balmer decrement $L_{\rm H\alpha}/L_{\rm H\beta} = 2.86$, assuming Case B recombination, $T_{\rm e} = 10\,000$ K and electron density $n_{\rm e} =$

[4]For a single dust screen, one has $A_V = 2.5\log(e)\tau_V$, but since PROSPECTOR uses two dust screens, the exact conversion between τ_V and A_V depends on the ratio between young and old stellar populations, where the former are attenuated by both the diffuse and 'birth-cloud' dust, while the latter are attenuated only by diffuse dust.

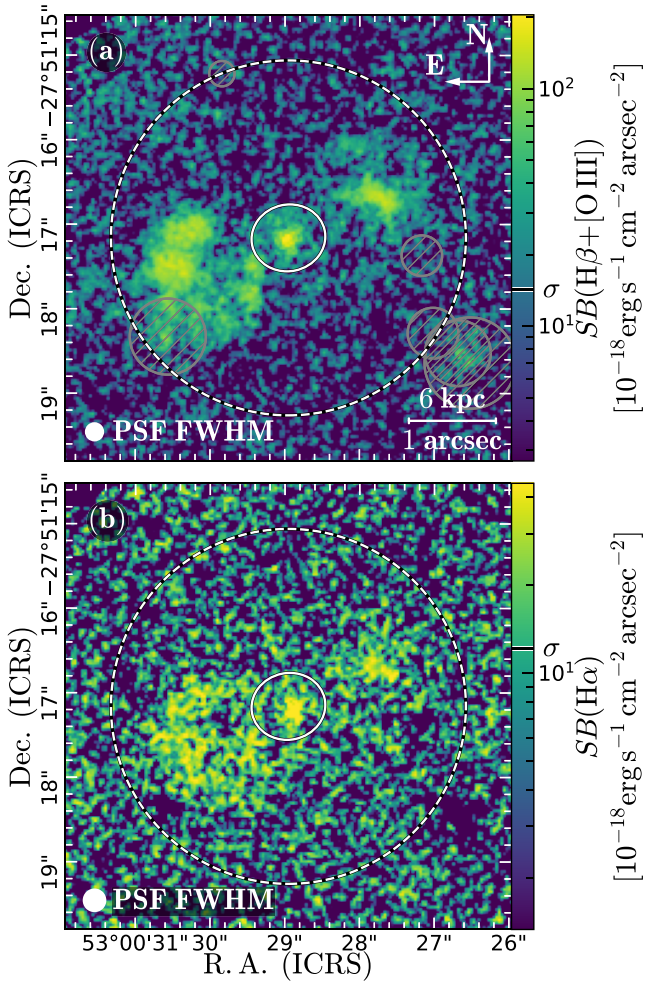

Figure 6. NIRCam-derived emission-line maps of Hβ and [O III]$\lambda\lambda$4959, 5007 (panel a), and Hα (panel b). The colourbar shows the 60th–99.9th percentile range, with the 1σ noise level highlighted by a horizontal mark. The dashed circle is the region where we estimate the total flux; the solid ellipse is excluded and is considered to be associated with the galaxy (Section 4). The observed [O III] luminosity of the nebula exceeds that of the host galaxy by an order of magnitude. Note the different morphology of the host galaxy in the two images; differential concentration of [O III]$\lambda\lambda$4959, 5007 versus Hα may indicate obscured AGN activity. The PSFs FWHM in *F*356*W* and *F*444*W* are indicated by the white circle.

100 cm^{-3}; Osterbrock & Ferland (2006). With this assumption, an [O III] doublet ratio of 2.98 and no dust attenuation, we estimate $L_{\rm O\,III\lambda5007} \sim 1.2 \times 10^{10}$ L$_\odot$ $= 4.6 \times 10^{43}$ erg s^{-1}. With this value, we derive $L_{\rm O\,III\lambda5007}/L_{\rm H\beta} \approx 5$, lower than the narrow-line regions of quasars at $z = 0.4$–0.7 (both obscured and unobscured; Liu et al. 2013; Liu, Zakamska & Greene 2014).

Alternatively, if we assume the typical [O III]λ5007/H $\beta \sim 10$ of quasar-illuminated nebulae (Liu et al. 2013, 2014; Lyu et al. 2025) or outflows (Scholtz et al. 2020), we would infer an Hβ luminosity of 1.2×10^9 L$_\odot$, 2 times lower than the prediction from the observed Hα luminosity. The grism spectra suggests that the contribution of [N II]$\lambda\lambda$6548, 6583 to the nebular emission is negligible (Section 3), which would imply some degree of dust attenuation. However, a weak continuum could also alter the line ratios, so confirming the presence of dust requires deeper, spatially resolved spectroscopy.

Regardless of the estimate of $L_{\rm H\beta}$, the resulting [O III]λ5007 luminosity is extremely high for a non-quasar galaxy; typical unobscured quasars at $z = 0.4$–0.7 have $L_{\rm [O\,III]\lambda5007} \approx 2.5 \times 10^9$ L$_\odot$ (Liu et al. 2014), but JADES-GS-518794 shows no trace of an active quasar at the centre of the host galaxy. Hainline et al. (2013) compared the [O III]λ5007 and rest frame 8-μm luminosity of a sample of 50 obscured quasars; using their empirical relation (their fig. 5), we infer that JADES-GS-518794 could have a flux density as high as $S_{50\,\mu\rm m} \sim 10$ μJy, which is in the range of predictions of our CIGALE AGN models (Fig. 5).

With $L_{\rm H\alpha} = 0.66 \times 10^{10}$ L$_\odot$, assuming no dust attenuation and all of the line emission arising from star formation, and adopting the Kennicutt & Evans (2012) conversion, the nebula would have a $SFR \sim 80$ M$_\odot$ yr^{-1}, which is larger than the host galaxy (Fig. 4c).

8 LARGE-SCALE ENVIRONMENT

Early massive galaxies, such as JADES-GS-518794, are thought to trace some of the most active star-forming regions in the Universe. As a result of this, dusty star-forming galaxies (DSFGs) and sub-millimetre galaxies (SMGs) have often been used to identify galaxy protoclusters at high redshifts (Chapman et al. 2009; Riechers et al. 2014; Umehata et al. 2015; Oteo et al. 2018; Long et al. 2020; Sun et al. 2024; Fudamoto et al. 2025). One reason for this is the growing evidence for accelerated galaxy evolution within overdense environments (e.g. Arribas et al. 2024; Helton et al. 2024a, b; Morishita et al. 2025). DSFGs and SMGs are some of the most extreme objects found at high redshifts, so it would make sense for these to be situated within an overdense region of galaxies.

Indeed, there is already spectroscopic evidence for an overdensity in GOODS-S around $z = 5.8$–5.9, based on Keck redshifts from Lyα emission for *i*-band drop galaxies in this redshift range (Bunker et al. 2003; Stanway et al. 2004a, b).

To explore the large-scale environment surrounding JADES-GS-518794, we searched for relatively bright galaxies ($m <$ 28.5 AB mag in *F*444*W*, adopting Kron photometry) that are consistent with the redshift of JADES-GS-518794 by using the v0.9.5 JADES GOODS-S photometric catalogue (Rieke et al. 2023). We measured photometric redshifts with EAZY (Brammer et al. 2008) following the methodology of Hainline et al. (2024) using CIRC1 photometry (0.10-arcsec radius) and adopting the redshift where the likelihood is maximized (χ^2 is minimized), which produced $z_{\rm phot} = 6.01$ for JADES-GS-518794. The median photometric redshift uncertainty at $z_{\rm phot} \approx 6$ is $\Delta z_{\rm phot} \approx 0.24$ (corresponding to velocity uncertainties of roughly 10 000 km s^{-1}). Photometric redshift uncertainties are measured as the difference between the 16th and 84th percentiles of the photometric redshift posterior distributions. We choose to not make any cut on the photometric redshift uncertainty since this would bias against dusty and quiescent galaxies like JADES-GS-518794 and the candidate satellite galaxy. Based on the typical photometric redshift uncertainty, we select galaxies that are within $\Delta z_{\rm phot}$ of JADES-GS-518794 (i.e. $5.77 < z_{\rm phot} < 6.25$). There is some evidence for the uncertainties on $z_{\rm phot}$ from EAZY being underpredicted, but investigating this possibility goes beyond the scope of this article. Following these selections, we are left with a photometric sample of $N = 998$ sources at $z_{\rm phot} \approx 6$. We identify nine sources within 2 arcsec from JADES-GS-518794, of which six were selected in the sample of 998; including these six sources in the clustering analysis would increase the significance of our results. However, since these sources are most likely gas clouds and not galaxies, we conservatively remove them from the sample.

Following the methodology outlined in Sandles et al. (2023) and Alberts et al. (2024), we utilize a kernel density estimator (KDE) to

estimate the underlying density field for the photometric sample. We assumed Gaussian kernels and optimize the assumed bandwidth (i.e. the smoothing scale) by maximizing the likelihood cross-validation quantity (Chartab et al. 2020). The optimized bandwidth for the photometric sample is 2.402 cMpc and corresponds to roughly 1.0 arcmin at the redshift of JADES-GS-518794. We further implement a correction factor to compensate for KDEs underestimating densities near the edge of footprints (Taamoli et al. 2024). We finally subtract the individual density values for each galaxy by the mean density value estimated across the entire field to ensure that only half of the photometric sample is classified as overdense.

8.1 A new candidate overdensity in GOODS-S

The adopted methodology using the KDE identifies two spatially distinct galaxy overdensities that have peak significance levels higher than 3σ, where σ is defined to be the standard deviation of the density values across the entire field. The former of these two overdensities is at RA 53.1297, Dec. −27.7854 with a peak density of 3.3 times that of a random volume. This peak corresponds to the spectroscopically confirmed galaxy overdensity JADES-GS-OD-5.928 (Helton et al. 2024b). The second of these overdensities is at RA 53.0239, Dec. −27.84233 with a peak density of 3.8 times that of a random volume. It consists of 44 galaxies (including JADES-GS-518794), with mean redshift $z_{\rm phot} = 5.99$ and a standard deviation of 0.04. The centre of this new overdensity is sufficiently far from previously known Ly α emitters (Stanway et al. 2004b) to be considered separate. If we include the six sources identified as clouds in the analysis, the significance would increase to 4.1 times the random value, and the number of galaxies would increase from 44 to 56 (since the size of overdensity also increases slightly). Our inferred centre is separated by only 2.760 cMpc (1.126 arcmin) from JADES-GS-518794 (at the centre of the overdensity we find a close group of five galaxies; Appendix B). However, since JADES-GS-518794 is near the edge of the footprint for which we have imaging from *HST* and *JWST*, it is possible that there is a substantial number of galaxies missed by our catalogue and therefore by the KDE. These missing galaxies would bias the KDE estimate of the peak density away from JADES-GS-518794 and towards the North, as observed. Nevertheless, while this overdensity is photometrically even more significant than JADES-GS-OD-5.928, it lacks spectroscopic confirmation and is thus considered a candidate overdensity.

Fig. 7 illustrates the spatial distribution of the $N = 992$ galaxy candidates in the photometric sample using points that are colour-coded by their photometric redshifts. These galaxy candidates are at $5.77 < z_{\rm phot} < 6.25$ in GOODS-S and are selected based on the available *HST* and *JWST* photometry. The underlying density field is estimated with a KDE and is illustrated by the contours. The contours increment by 1σ, where σ corresponds to the standard deviation of the density values across the entire field. The purple contour represents a significance level of 3σ, which is the threshold we adopt to identify galaxy overdensities. The gold star illustrates the location of JADES-GS-518794, which falls near the edge of the JADES footprint, shown by the thick black line.

Given the proximity with one of the extreme galaxy overdensities identified here, it is possible that the large-scale environment is in some part linked to the extended line-emitting nebulae surrounding JADES-GS-518794. Environmental effects may have caused accelerated galaxy evolution and the creation of an AGN within JADES-GS-518794 that is responsible for the expelled gas, or they could have increased the rate of mergers and interactions that has tidally stripped the gas from JADES-GS-518794. Either way, it is likely that environment has played an important role, and it is possible that JADES-GS-518794 is a brightest cluster galaxy (BCG) in the making. Future spectroscopic observations will provide more information about the large-scale structure surrounding JADES-GS-518794 and the impact of environment.

8.2 Environment impact on galaxy properties

To gauge the possible effects of large-scale environment on the SFH of JADES-GS-518794, in Fig. 8 we compare the properties of the 56 galaxies in the candidate overdensity (purple empty histogram) to the control sample of 914 galaxies that are not in any known overdensity (filled grey histogram).[5] To test if the two samples are consistent with being drawn from the same distribution, we use a Kolmogorov–Smirnov (KS) test (but we also report the *P*-value from Anderson–Darling, AD test). Fig. 8(a) compares the distributions of *F*444*W* magnitude, which at $z \sim 6$ traces the rest-frame red optical, including H α emission. We find no statistical evidence of a difference between the two distributions. Similarly, we find no evidence of a difference in the *F*410*M*–*F*444*W* colour (Fig. 8b), which at $z \sim 6$ traces primarily the EW of H α (equation 3; [N II]$\lambda\lambda$6548, 6583 and [SII]$\lambda\lambda$6716, 6731 are much fainter than H α at $z > 5$; Cameron et al. 2023; Sandles et al. 2024). In contrast, we find strong evidence of a colour difference in *F*200*W*–*F*277*W*, the two NIRCam bands bracketing the Balmer break at $z \sim 6$ (Fig. 8c; *P*-value $P < 10^{-4}$). This remarkable difference in *F*200*W*–*F*277*W* colour suggests that galaxies in overdensities have on average older light-weighted stellar-population ages than galaxies in non-overdense regions, consistent with an earlier start of their SFHs. Stellar metallicity could also play some role, due to the physical degeneracy between stellar age and metallicity, but a significant metallicity enhancement on large scales seems less likely at these early epochs (but has been observed in clusters of galaxies at lower redshifts $z = 0.35$; Gupta et al. 2016). A contribution from emission lines (chiefly [O II]$\lambda\lambda$3726, 3729 and [Ne III]λ3869) is also possible, but it is unlikely to be the dominant effect. First, the large values of *F*200*W*–*F*277*W* (reaching 1 mag; Fig. 8c) strongly suggest that a difference in continuum shape must be present, at least in some galaxies (see also discussion about the Balmer break in JADES-GS-518794; Section 5.1). Second, we detect no enhancement in *F*410*M*–*F*444*W* (Fig. 8b), so the EW of emission lines between galaxies in overdensities and the control must be similar. Therefore, increasing *F*200*W*–*F*277*W* at fixed *EW*(Hα) requires very low ionization and/or high metallicity, which seems unlikely at $z \sim 6$ and on large scales. If the *F*200*W*–*F*277*W* is pointing to stronger Balmer breaks, then this would imply a higher average mass-to-light ratio for galaxies in overdensities, meaning that the similar distribution in *F*444*W* magnitude may hide different distributions in $M_\star$, that is, at fixed luminosity, galaxies in the overdensity are more massive than those in the control sample.

To better characterize the physical properties of the galaxies in the candidate overdensity, we use PROSPECTOR β (Wang et al. 2023a), a version of PROSPECTOR (Johnson et al. 2021) optimized for redshift recovery. PROSPECTOR β utilizes a series of galaxy evolution priors, including a stellar mass prior derived in Leja et al. (2020), a prior on galaxy number density as a function of redshift, and the continuity prior for the SFH described in Section 5, but here with seven logarithmically spaced time bins. In addition, there is a mass-dependence on the SFH prior, where the start of each age bin is shifted

[5]For a test of small-scale environment effects, see Appendix B.

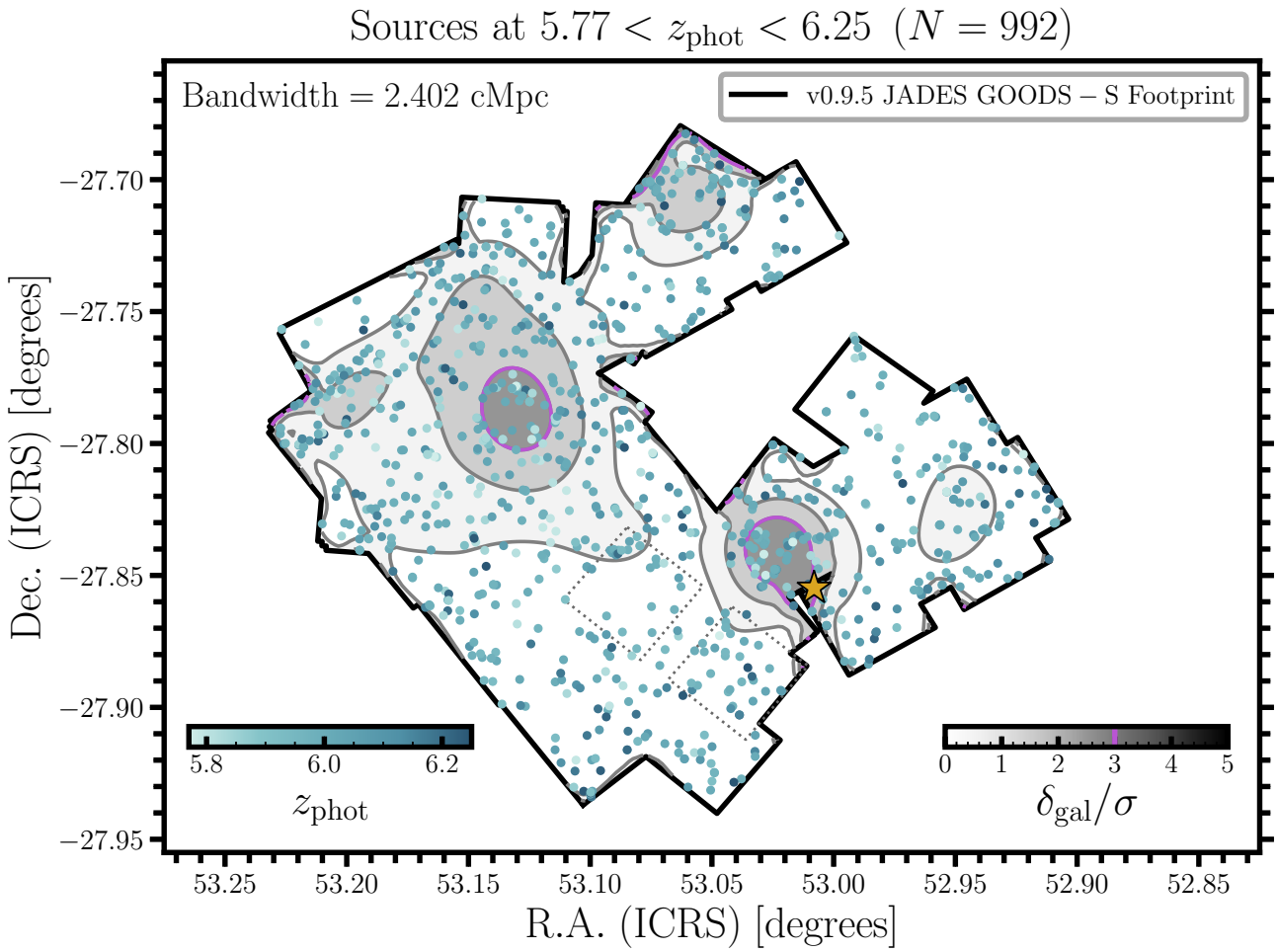

Figure 7. The spatial distribution of the $N = 992$ galaxy candidates in the photometric sample using points that are colour-coded by their photometric redshifts. These galaxy candidates are at $5.77 < z_{\rm phot} < 6.25$ in GOODS-S and are selected based on the available *HST* and *JWST* photometry. The thick black polygon is the GOODS-S NIRCam footprint of JADES, while the dotted grey contours trace the JADES Origins Field, the deepest NIRCam imaging. The underlying density field is estimated with a KDE and is illustrated by the contours. The contours increment by 1σ, where σ is the standard deviation of the density values across the entire field. The purple contour represents a significance level of 3σ, which is the threshold we adopt to identify galaxy overdensities. We identify two spatially distinct galaxy overdensities. One of these corresponds to a spectroscopically confirmed galaxy overdensity in GOODS-S (JADES-GS-OD-5.928 from Helton et al. 2024b). The other one of these is only 2.311 cMpc (0.943 arcmin) in separation from JADES-GS-518794. The gold star illustrates the location of JADES-GS-518794, which falls near the edge of the JADES footprint, shown by the black line.

based on the stellar mass, as described in Wang et al. (2023a). We refer the reader here for a complete description of the PROSPECTOR β priors. For consistency with the clustering analysis, the redshift is fixed to the photometric redshift inferred with EAZY.

The distribution of the resulting galaxy properties is shown in Fig. 9. We find no evidence for a difference in $M_\star$ between members and non-members of the overdensity (according to the KS and AD tests, respectively; panel a). Similarly, we find no difference in specific SFR (panel b, in agreement with no difference in $F410M$–$F444W$), and no difference in the mass-weighted age and dust attenuation properties (panels c and d). The lack of difference in mass-weighted age maybe due to the known difficulty of measuring accurate mass-weighted stellar properties for young galaxies – particularly when relying on rest-frame UV and optical wavelengths. Alternatively, the constraining power of our small photometric sample may be insufficient to overcome the constraints from the prior probabilities assumed by PROSPECTOR β.

9 DISCUSSION

The discovery of a large, 25-kpc diameter emission-line nebula at $z = 5.89$ underscores the combined power of medium- and wide-band photometry to identify and characterize extended line-emitting nebulae (Zhu et al. 2025). While there are other large emission-line regions within the 300-arcmin^2 area of the GOODS fields covered by JADES (Scholtz et al. 2020; D'Eugenio et al. 2024; Zhu et al. 2025), this nebula is unique at such early times as $z = 5.89$. However, building a larger sample for this kind of bright and rare source requires a large-area medium-band survey and deep follow-up with spectroscopy.

For the case of JADES-GS-518794, while only further observations can give definitive answers, the galaxy location at the centre of the nebula and at a photometric redshift consistent with the nebular spectroscopic redshift leaves little doubt about the physical association of this system.

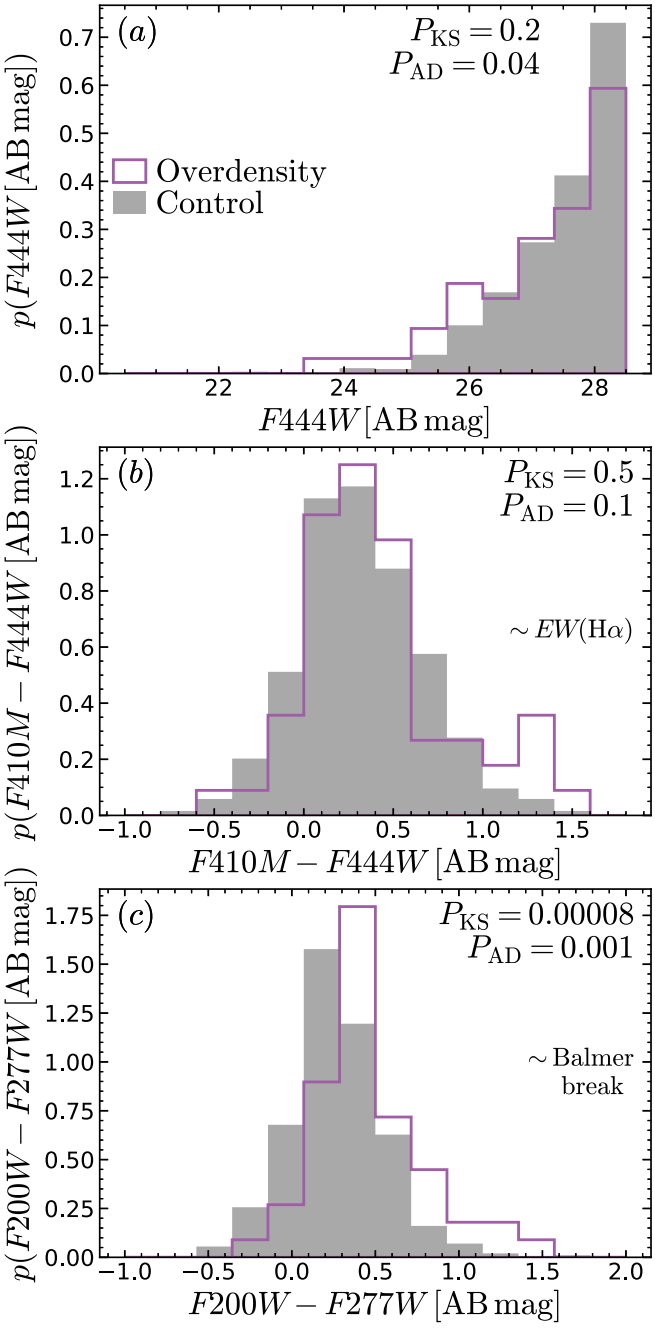

Figure 8. Comparing the properties of 56 galaxies in the candidate overdensity (purple) to the control sample of 914 galaxies not in any overdensity (filled grey). We report the *P*-value P of the null hypothesis that the two samples are drawn from the same distribution (according to the KS and AD tests). We find no difference in $F444W$ magnitude and in $F410M$–$F444W$ colour, but a statistically significant excess in $F200W$–$F277W$ colour (tracing the Balmer break at $z \sim 6$), likely indicating that galaxies in overdensities have on average older light-weighted ages.

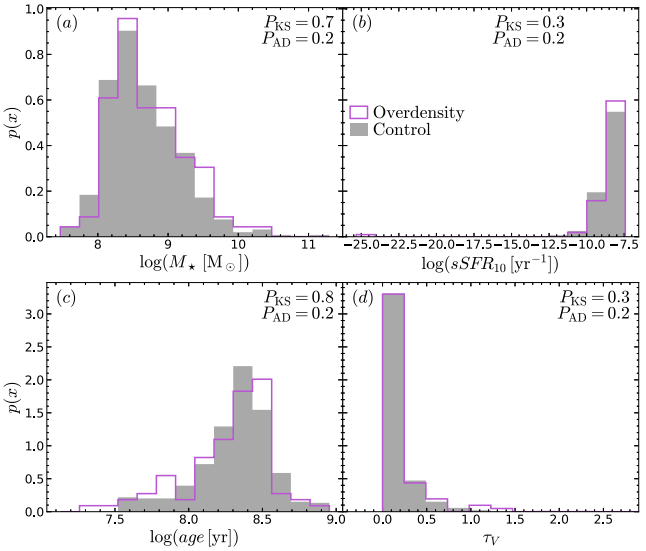

Figure 9. Comparing the physical properties of galaxies in the candidate overdensity (purple) to a control sample of galaxies not in any overdensity (filled grey). We report the *P*-value P of the null hypothesis that the two samples are drawn from the same distribution (according to the KS and AD tests), but find no evidence for differences in the physical properties between galaxies in the overdensity and the control sample.

9.1 Large-scale environment

The galaxy and its nebula belong to a candidate large-scale galaxy overdensity, with a significance higher than JADES-GS-OD-5.928 (which has been spectroscopically confirmed; Helton et al. 2024b). JADES-GS-518794 is located at the same redshift as the candidate overdensity and within a projected distance of 2.3 cMpc from the peak density (Section 8). While the depth of the JADES imaging varies significantly across the survey footprint in GOODS-S, using a magnitude cut in $F444W$ magnitude of 28.5 mag and no cut on the photometric redshift uncertainties should remove any bias due to varying survey depth. Indeed, we find that the highest-significance peak is not in the deepest region of the field (which is the JADES Origins Field; Eisenstein et al. 2023b; dotted grey lines in Fig. 7). Because overdensities as large as the one considered here are far from having collapsed, we do not expect the environment-driven processes seen on Mpc scales at $z \lesssim 2$ to be already in place (e.g. Ji et al. 2018; Donnari et al. 2019, 2021). However, being part of an overdensity, the galaxy may still be subject to other effects, such as an earlier-than-average gravitational collapse, a higher-than-average ionization fraction of the intergalactic medium (Lu et al. 2024; Whitler et al. 2024), and higher gas metallicity.

Previous studies have found an excess of galaxies with low-EW Hα + [N II] emission in two galaxy overdensities at $z = 5.7$ (Morishita et al. 2025, 25 ± 7 per cent versus 6 ± 2 per cent for non-overdensity galaxies), but we find no difference in the $F410M$–$F444W$ colour (tracing Hα EW) distribution between galaxies inside or outside the overdensity (Fig. 8b). The discrepancy could be in part due to galaxies in overdensities displaying a broader range of EWs, due to environment-driven processes acting to both enhance and suppress star formation – as also discussed in Morishita et al. (2025). Another possible explanation for the discrepancy are different methods: Morishita et al. (2025) use deep NIRSpec and NIRCam/WFSS spectroscopy, while this work relies on photometry only. Indeed, the observations from Morishita et al. (2025) reach $EW = 30$–100 Å, which would correspond to a $F410M$–$F444W$ colour of ~ 0.2 mag. Given the survey depth of the JADES medium-depth regions (Eisenstein et al. 2023a; D'Eugenio et al. 2025b), this effect is too subtle to capture in individual galaxies at the faint end of our sample (28.5 mag in $F444W$), and would correspond to only a 3σ colour difference at 27.5 mag.

However, Morishita et al. (2025) also find that their low-EW galaxies have evidence of Balmer breaks (their D_e4000 index maps very well to the definition of Balmer-break index used here). This result is in qualitative agreement with the observations from Naidu et al. (2024). Our work presents statistical evidence for galaxies in the candidate overdensity having redder *F*200*W*–*F*277*W* colour than typical galaxies at the same redshift. We discussed that a difference in emission-line properties is unlikely, given the lack of difference in *F*410*M*–*F*444*W* (tracing primarily $EW(\mathrm{H}\alpha)$), which together with the redder *F*200*W*–*F*277*W* colour would imply a systematically stronger [O II]λλ3726, 3729 emission. We therefore interpret the colour difference as evidence for galaxies in overdensities having stronger Balmer breaks (Section 8). This could in turn be due to older light-weighted ages and/or higher metallicities. While higher gas metallicities in dense environments than in the field have been measured up to $z = 0.35$ (Gupta et al. 2016), there is yet no direct evidence for metallicity enhancements at $z \sim 6$. Besides, a higher *stellar* metallicity would almost certainly imply much larger stellar masses to explain the chemical enrichment. In contrast, older stellar population ages would naturally fit in the standard ΛCDM model, where overdense regions start to collapse earlier, giving their galaxies a head start in the SFH. Deep medium-band imaging (e.g. Trussler et al. 2025) or follow-up spectroscopy (e.g. Looser et al. 2024b; Baker et al. 2025b) are required to confirm the presence of these Balmer breaks and to investigate their physical cause.

On the spatial scales of the CGM (tens of kpc), we may already be seeing environment-driven effects, as already witnessed at $z \sim 3.5$ (Alberts et al. 2024). The centre of the overdensity (Fig. B1) contains six galaxies, which as a sample stand out in both *F*444*W* magnitude and *F*200*W*–*F*277*W* colour (Fig. B2). This suggests that large overdensities may be connected to the early formation of massive galaxies in their centres, consistent with the finding that massive, dusty star-forming galaxies are good tracers of galaxy proto-clusters (Daddi et al. 2009; Riechers et al. 2010; Oteo et al. 2018; Pavesi et al. 2018; Drake et al. 2020), including at high redshifts (Smolčić et al. 2017; Lewis et al. 2018; Hashimoto et al. 2023; Arribas et al. 2024). However, neither JADES-GS-518794 nor the galaxies nearest to the centre of the overdensity are particularly dusty, so we could be witnessing the assembly phase before the dusty starburst event.

An excess of Balmer-break galaxies in the densest environments may point to the synergy between internal feedback and environment. Star formation or AGN-driven feedback can temporarily interrupt star formation (Ceverino, Klessen & Glover 2018; Lovell et al. 2023), while the central galaxy could be appropriating the gas reservoir of the satellite, preventing re-accretion and rejuvenation (Gelli et al. 2025). Large-scale AGN outflows like the one seen around JADES-GS-518794 – if they are sufficiently common – could also impact low-mass satellites, for instance by triggering a starburst and accelerating the depletion and/or removal of gas (Croft et al. 2006; Inskip et al. 2008; Salomé, Salomé & Combes 2015).

The possible presence of a satellite (JADES-GS-518709) with a strong Balmer break and a mass ratio of 1:6 seems significant (Section 5.2). This is because galaxies with strong Balmer breaks (i.e. having had negligible star formation for hundreds of Myr) with masses $10^9 \lesssim M_\star \lesssim 10^{10}$ M$_\odot$ are rare at $z > 3$ (Baker et al. 2025a; Trussler et al. 2025). If confirmed, the coincidence would be significant, suggesting that 'environment pre-processing' may be already at work in the first billion years after the big bang (Alberts et al. 2024). It is worth remarking that the best-fitting EAZY photometric redshift of JADES-GS-518709 is $z_{\mathrm{phot}} = 4.4$, therefore our results should be considered with caution (Section 5.2). However, the absence of emission lines and possible contamination of the photometry by the brighter central could be biasing this measurement. Besides, such a low-mass quiescent galaxy, if confirmed to be at $z = 4.4$, would be remarkably isolated, which would be even more extraordinary than a satellite at $z = 5.89$. Either way, spectroscopic confirmation is required.

9.2 Main galaxy

The galaxy SED shows strong evidence of a break or line excess between *F*200*W* and *F*277*W* (Fig. 4a). If due to line emission, this would imply a rest-frame $EW([\mathrm{O\,II}]\lambda\lambda3726, 3729) < -250$ Å, extremely high for [O II]λλ3726, 3729 (Blanton & Lin 2000; Yan et al. 2006). If true, such a high-magnitude EW is certainly worth studying. However, our fiducial interpretation is that the difference between *F*200*W* and *F*277*W* is due to a Balmer break, implying that evolved stars are present and dominate the mass budget. This is supported by our SED models, which still find a Balmer break even for the highest-magnitude $EW([\mathrm{O\,II}])$ explored. While remarkable, a strong Balmer break at $z = 5.89$ is not implausible, with the most distant such case being at $z = 7.3$ (Weibel et al. 2025), and weaker breaks at even higher redshifts (Kuruvanthodi et al. 2024; Looser et al. 2024b; Baker et al. 2025b), and some $z = 6$ cases even pre-dating *JWST* (Eyles et al. 2005, 2007). With $M_\star \sim 10^{10}$ M$_\odot$, JADES-GS-518794 appears to be fairly massive (for $z \sim 6$), only 2 times lower than the first massive, quiescent galaxies (Weibel et al. 2025) and comparable to the knee of the galaxy mass function at $z = 6$ (Weaver et al. 2023; Weibel et al. 2024). We remark that $M_\star$ is also subject to systematic uncertainties of 0.3 dex (as found by e.g. Conroy, Gunn & White 2009; Muzzin et al. 2009; Pacifici et al. 2023). These uncertainties arise due to the inability of photometry in the rest-frame UV – optical to fully break the degeneracy between age and dust, or age and metallicity (e.g. Trager et al. 1998; Nersesian et al. 2024). As for the SFH, SED modelling suggests that the galaxy may have experienced an upturn in the most recent 10 Myr (Fig. 4c). This upturn is required to explain the medium-band excess in *F*335*M* versus *F*356*W*, itself due to H β and [O III]λλ4959, 5007 line emission. We caution that by construction, our PROSPECTOR set-up interprets this emission as due to star formation photoionization, hence the upturn in SFR. However, AGN photoionization and shocks are equally plausible drivers of the observed photometric excess but are not included in our model. For this reason, the SFR upturn in the last 10 Myr is not conclusive. To confirm if the SFR in JADES-GS-518794 is really resurrecting, we need 3–4 μm spectroscopy. In contrast, the downturn 10–100 Myr prior to observation is driven by the Balmer break and shape of the stellar continuum, so it should be fairly robust against AGN- and shock-driven emission. The large scatter in the SFH during the period 10–100 Myr is due to the photometry being unable to precisely pinpoint in time the epoch of the SFR downturn. However, the presence of a downturn seems robust (Section 5.1; Fig. 4d). A case of a strong shock in a galaxy with a Balmer break was recently identified at $z = 4.7$ by the WIDE Survey (Maseda et al. 2024; D'Eugenio et al. 2025b). However, the similarity is not complete, because while their galaxy presents very strong [O II]λλ3726, 3729 emission, its [O III]λλ4959, 5007 emission is remarkably weak and the SFH does not display any substantial downturn (D'Eugenio et al. 2025b).

9.3 Origins of the emission-line nebula

The large physical size, velocity and high luminosity of the nebula suggest that its origin may be linked to AGN-driven outflows and AGN photoionization (Lintott et al. 2009). While some extreme

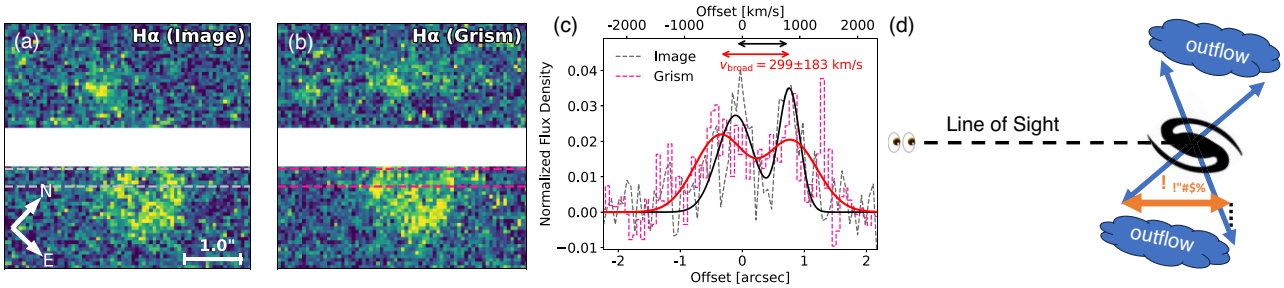

Figure 10. Evidence of kinematic broadening supports the biconical outflow interpretation for the emission-line nebula. Panel (a): Hα emission constructed from *F*444*W* to *F*410*M* image, aligned with dispersion direction. Panel (b): Hα emission in the 2D grism spectra. Panel (c): Hα profiles in the image (grey) and grism (pink) extracted from the apertures shown by the dashed lines in panels (a) and (b). Velocity offset in the slitless spectrum is degenerate with spatial offset. By fitting the profiles with double Gaussian functions we obtain evidence of kinematic broadening of ~ 300 km s^{-1}. This is consistent with the expectation from biconical gas outflow as illustrated by the cartoon in panel (d).

starbursts are also thought to drive massive, extended outflows (Rupke et al. 2019), the SFH in JADES-GS-518794 disfavours this interpretation. Still, tidal disruption or strong shocks are still possible alternatives to the AGN scenario and will require spectroscopy (e.g. D'Eugenio et al. 2025b) and ideally integral-field spectroscopy (e.g. Venturi et al. 2023; Saxena et al. 2024) for a definitive assessment. Still, with the data in hand, several lines of evidence favour AGN outflows. First, the extremely compact morphology of Hβ + [O III] in the galaxy itself supports the presence of a point source or extremely compact narrow-line region (Fig. 6). When we consider the tentative MIR fluxes from *Spitzer* and the MIRI detection at 15 µm (Section 6), the data are best reproduced by a model with an obscured AGN (Fig. 5). The similar reduced-χ^2 values between the AGN and no-AGN models are driven by the large discrepancy around the Balmer break, likely due the SFH parametrization we used in CIGALE. Nevertheless, the two models are formally consistent with the data, so we consider this circumstantial evidence only. The presence of an AGN, if confirmed, would resonate with recent outflows, though admittedly mergers and tidal disruption could also trigger an AGN (Ellison et al. 2025; Perna et al. 2025). The presence of two clouds symmetrically located on either side of the galaxy also favours an AGN origin, as do their convex shapes, reminiscent of bow shocks and bubbles (Nelson et al. 2019; see e.g. Cresci et al. 2023; Veilleux et al. 2023; Venturi et al. 2023 for observational evidence). From the grism spectrum, we find some indications that the Hα emission from the East cloud is broader than in the NIRCam image (cf. pink versus black lines in Fig. 10c). This additional broadening corresponds to a velocity dispersion of ~ 300 km s^{-1}, consistent with the expected kinematic broadening from conical outflow geometry (Fig. 10). However, this will need to be further confirmed with NIRSpec/IFS data at higher spectral resolution and sensitivity. A final argument in favour of an AGN is the high Hα luminosity; in the merger/tidal disruption scenario, the Hα luminosity would imply a very high SFR of 80 M$_\odot$ yr^{-1} in the nebula, which should be associated with easily detectable stellar continuum light, yet very little continuum is seen. Extreme emission-line galaxies are generally found to be compact (Withers et al. 2023; Boyett et al. 2024), unlike our case. The SFR value is very large for a tidally disrupted satellite; for comparison, the extended emission-line region in the Tusitala group, around the much more massive galaxy COS20115 ('Jekyll', $M_\star = (0.9\text{–}1.8) \times 10^{11}$ M$_\odot$; Glazebrook et al. 2017; Schreiber et al. 2018; Pérez-González et al. 2024) has a total equivalent SFR that is 3 times lower, raising the question of whether JADES-GS-518794, which is 10 times less massive than Jekyll, could disrupt 3 times more gas. Moreover, the high line-to-continuum ratio in the clouds (which SED modelling struggles to reproduce, Section 5.3) imply extremely young mass-weighted stellar ages (of order ~ 1 Myr). These young ages are implausible over such an extended region, because the speed of the signal needed to synchronize star formation over 10 kpc would be of order 10^4 km s^{-1}. This is much larger than the outflow velocities typically measured on comparable scales.

While the tidal disruption explanation seems unlikely, our favoured AGN-outflows scenario is not without problems. Powerful outflows are generally associated with intense accretion activity, but JADES-GS-518794 appears to be a fairly faint, spatially resolved target, unlike bright and point-like quasars. A similar but less extended and luminous case has been recently found near the faint QSO HSC J2239+0207 (Lyu et al. 2025). The comparison with Lyu et al. (2025) makes our nebula even more puzzling, since their nebula is less extended and luminous, while the central galaxy is at least a QSO, unlike JADES-GS-518794. The MIR constraints place an upper limit on the AGN luminosity of $L_{\rm bol} \lesssim 10^{45.8}$ erg s^{-1}, significantly lower than bright quasars. Still, observations from the local Universe show that AGN can fade by orders of magnitude over time-scales of a few Myr (Finlez et al. 2022), so even though JADES-GS-518794 is not a bright QSO, we could be observing a relic nebula (Lintott et al. 2009). Future MIRI observations are necessary to place more stringent constraints on the obscured AGN.

9.4 A link with quenching?

Intriguingly, SED modelling suggests that the galaxy may have experienced a downturn in recent star formation (Fig. 4c). If confirmed, this scenario may be linked to the presence of the large nebula. In the absence of strong ionizing emission (as suggested by the faint nature of JADES-GS-518794), the lifetime of collisionally excited emission should be fairly short, of order 10^4 yr. In addition, the velocity offset between the East and West clouds is $\Delta v \approx 800$ km s^{-1} (Section 3). Interpreting the clouds as originating from the galaxy, and using the projected separation of 6 kpc between JADES-GS-518794 and the highest-brightness cloud, we can derive an outflow age of at least ≈ 15 Myr, clearly longer than the cooling time, and thus requiring external photoionization (for example, from a faded AGN in JADES-GS-518794), or a local source of power like fast shocks. The age of the putative outflow matches well the recent upturn in the SFH (Fig. 4d).

Could massive outflow events be linked to galaxies quenching? Most definitions of quiescence require no star formation for hundreds of Myr; assuming the visibility time for the cloud to be 15 Myr, galaxies like JADES-GS-518794 could be the progenitors of 10×

larger volume densities of quiescent galaxies, meaning that extended, luminous nebulae may be a common but short-lived evolutionary phase around massive galaxies at these high redshifts. The presence of possible signatures of a recent merger (Section 4) resonate with the merger-then-quenching scenario (Hopkins et al. 2008), where a major merger increases both the SFR and the accretion rate of the supermassive black hole until a 'blowout' phase that precedes quenching. If we are truly witnessing this short-lived blowout phase in JADES-GS-518794, this would have implications for our understanding of how SMBH feedback affects the host galaxy and causes quenching. So far there are only few observations of the circumgalactic medium around massive, quiescent galaxies at $z > 3$; however, where data are sufficiently deep, all these systems appear to have some more or less extended emission-line regions (D'Eugenio et al. 2024; Pérez-González et al. 2024 using NIRSpec/IFS; Pascalau et al. 2025, using NIRCam). This may point to a connection between these extended emission-line regions and neutral-gas outflows, which have been confirmed in several quiescent galaxies around and before cosmic noon (Davies et al. 2024), including the galaxy from D'Eugenio et al. (2024), where NIRSpec/IFS confirms the simultaneous presence of both extended ionized-gas emission and neutral outflows with high mass-outflow rate (Scholtz et al. 2024).

Unfortunately, distinguishing between the scenarios presented earlier is impossible with photometry alone, but with *JWST* integral field spectroscopy capable of revealing the chemical and kinematic properties of the nebula, the key to unlocking many of the open questions surrounding JADES-GS-518794 lies within reach.

10 SUMMARY AND CONCLUSIONS

In this work, we report the discovery of a large and luminous line-emitting nebula around a massive galaxy at $z = 5.89$ (Fig. 1). The galaxy and nebula have consistent photometric redshifts, driven by the Lyα break and photometric excess driven by strong emission lines. The nebula is confirmed spectroscopically using NIRCam/WFSS from SAPPHIRES (Fig. 2), which detects Hα at a mean redshift $z_{\rm spec} = 5.89 \pm 0.01$.

(i) SED modelling with PROSPECTOR (Fig. 4b) shows that the central galaxy JADES-GS-518794 has a stellar mass $\log(M_\star/{\rm M}_\odot) = 10.1^{+0.1}_{-0.2}$, near the knee of the mass function. In addition, the SFH shows a drop in star formation (10–100 Myr before observation, causing the observed Balmer break) followed by a recent upturn (powering the emission lines; Fig. 4d).

(ii) The emission-line regions cannot be modelled satisfactorily with our PROSPECTOR setup, implying these are gas clouds and not galaxies (Figs 4e and j).

(iii) The galaxy has a possible nearby satellite JADES-GS-518709 (Figs 1a and 4g). If confirmed, this would have a strong Balmer break (Fig. 4i). Its coincidence with JADES-GS-518794 would imply short-range interactions can enable or even cause quenching at $z \gtrsim 5.89$.

(iv) SED modelling with CIGALE does not require an AGN, but places a limit on the AGN luminosity of $\log(L_{\rm bol}\,[{\rm erg\ s^{-1}}]) < 45.8 \pm 0.6$ dex.

(v) The size, shape, kinematics, and high luminosity of the nebula ($L_{[{\rm O\,III}]\lambda5007} = 4.6 \times 10^{43}$ erg s^{-1}, Section 7) suggest a link with AGNs.

(vi) JADES-GS-518794 is found ~ 2 cMpc from the centre of a candidate galaxy overdensity (Fig. 7). This coincidence suggests a link between the massive nature of the galaxy and its membership into the overdensity (Section 8.1).

(vii) When compared to a control sample of coeval galaxies, the members of the overdensity have redder $F200W$–$F277W$ colour, suggesting a stronger Balmer break strength and pointing to an earlier formation of galaxies in the overdensity (Section 8.2, Fig. 8).

(viii) We speculate about a possible link between the presence of such a remarkable nebula and the downturn in SFR, possible evidence of a short lived 'blowout' phase before the onset of quiescence.

Future observations with *JWST* are required to fully understand the nature of this source, and its significance in the broader context of galaxy evolution.

ACKNOWLEDGEMENTS

FDE, RM, IJ, GCJ, DP, and JS acknowledge support by the Science and Technology Facilities Council (STFC), by the ERC through Advanced Grant 695671 'QUENCH', and by the UKRI Frontier Research grant RISEandFALL. RM also acknowledges funding from a research professorship from the Royal Society. SA and MP acknowledge grant PID2021-127718NB-I00 funded by the Spanish Ministry of Science and Innovation/State Agency of Research (MICIN/AEI/ 10.13039/501100011033). MP also acknowledges support from the Programa Atracción de Talento de la Comunidad de Madrid via grant 2018-T2/TIC-11715. SC and GV acknowledge support by European Union's HE ERC Starting Grant No. 101040227 - WINGS. ECL acknowledges support of an STFC Webb Fellowship (ST/W001438/1). ALD thanks the University of Cambridge Harding Distinguished Postgraduate Scholars Programme and Technology Facilities Council (STFC) Center for Doctoral Training (CDT) in Data intensive science at the University of Cambridge (STFC grant number 2742605) for a PhD studentship. EE, DJE, BER, and YZ acknowledge the *JWST*/NIRCam contract to the University of Arizona NAS5-02015. DJE was supported as a Simons Investigator. YF was supported by JSPS KAKENHI Grant Numbers JP22K21349 and JP23K13149. BER acknowledges support from *JWST* Program 3215. AJB acknowledges funding from the 'FirstGalaxies' Advanced Grant from the European Research Council (ERC) under the European Union's Horizon 2020 research and innovation programme (Grant agreement No. 789056). IJ and DP also acknowledge support by the Huo Family Foundation through a P.C. Ho PhD Studentship. PGP-G acknowledges support from grant PID2022-139567NB-I00 funded by Spanish Ministerio de Ciencia e Innovación MCIN/AEI/10.13039/501100011033, FEDER, UE. ST acknowledges support by the Royal Society Research Grant G125142. The research of CCW was supported by NOIRLab, which is managed by the Association of Universities for Research in Astronomy (AURA) under a cooperative agreement with the National Science Foundation. HÜ acknowledges funding by the European Union (ERC APEX, 101164796). Views and opinions expressed are however those of the authors only and do not necessarily reflect those of the European Union or the European Research Council Executive Agency. Neither the European Union nor the granting authority can be held responsible for them. JAAT acknowledges support from the Simons Foundation and *JWST* programme 3215. Support for programme 3215 was provided by NASA through a grant from the Space Telescope Science Institute, which is operated by the Association of Universities for Research in Astronomy, Inc., under NASA contract NAS 5-03127.

This work made use of the High Performance Computing (HPC) resources at the University of Arizona, which are funded by the Office of Research Discovery and Innovation (ORDI), Chief Information Officer (CIO), and University Information Technology Services

(UITS). This work made extensive use of the freely available Debian GNU/Linux operative system. We used the ⟨0:sc ⟩python⟨/0:sc⟩ programming language (van Rossum 1995), maintained and distributed by the Python Software Foundation. We made direct use of Python packages ASTROPY (Astropy Collaboration 2013), CORNER (Foreman-Mackey 2016), EMCEE (Foreman-Mackey et al. 2013), JWST (Alves de Oliveira et al. 2018), MATPLOTLIB (Hunter 2007), NUMPY (Harris et al. 2020), PPXF (Cappellari & Emsellem 2004; Cappellari 2017, 2022), PROSPECTOR (Johnson et al. 2021) v2.0, PYTHON-FSPS (Johnson et al. 2023), and SCIPY (Jones et al. 2001). We also used the softwares FSPS (Conroy et al. 2009; Conroy & Gunn 2010), TOPCAT, (Taylor 2005), FITSMAP, and DS9 (Joye & Mandel 2003).

DATA AVAILABILITY

This work is based on observations made with the NASA/ESA/CSA *James Webb Space Telescope*. Raw data were obtained from the Mikulski Archive for Space Telescopes at the Space Telescope Science Institute, which is operated by the Association of Universities for Research in Astronomy, Inc., under NASA contract NAS 5-03127 for *JWST*. These observations are associated with programmes PID 1180, 1210, 1286, 1287, 1895, 1963, 3215, 4540, and 6434. A new public release of the reduced images and photometric catalogues from PIDs 1180, 1210, 1286, 1287, and 3215 will be presented in JADES Collaboration (in preparation).

REFERENCES

Alberts S. et al., 2024, ApJ, 975, 85
Alves de Oliveira C. et al., 2018, in Proc. SPIE Conf. Ser. Vol. 10704, Observatory Operations: Strategies, Processes, and Systems VII. SPIE, Bellingham, p. 107040Q
Arribas S. et al., 2024, A&A, 688, A146
Astropy Collaboration, 2013, A&A, 558, A33
Baker W. M. et al., 2024, MNRAS, 534, 30
Baker W. M. et al., 2025a, MNRAS, 539, 557
Baker W. M. et al., 2025b, A&A, 697, A90
Balogh M. L., Morris S. L., Yee H. K. C., Carlberg R. G., Ellingson E., 1999, ApJ, 527, 54
Banerji M., Alaghband-Zadeh S., Hewett P. C., McMahon R. G., 2015, MNRAS, 447, 3368
Belli S. et al., 2024, Nature, 630, 54
Binggeli C. et al., 2019, MNRAS, 489, 3827
Binney J., 2004, MNRAS, 347, 1093
Blanton M., Lin H., 2000, ApJ, 543, L125
Bluck A. F. L., Maiolino R., Brownson S., Conselice C. J., Ellison S. L., Piotrowska J. M., Thorp M. D., 2022, A&A, 659, A160
Bluck A. F. L., Piotrowska J. M., Maiolino R., 2023, ApJ, 944, 108
Bower R. G., Benson A. J., Crain R. A., 2012, MNRAS, 422, 2816
Boyett K. et al., 2024, MNRAS, 535, 1796
Brammer G. B., van Dokkum P. G., Coppi P., 2008, ApJ, 686, 1503
Bruzual G., Charlot S., 2003, MNRAS, 344, 1000
Bunker A. J., Stanway E. R., Ellis R. S., McMahon R. G., McCarthy P. J., 2003, MNRAS, 342, L47
Byler N., Dalcanton J. J., Conroy C., Johnson B. D., 2017, ApJ, 840, 44
Calzetti D., Armus L., Bohlin R. C., Kinney A. L., Koornneef J., Storchi-Bergmann T., 2000, ApJ, 533, 682
Cameron A. J. et al., 2023, A&A, 677, A115
Cappellari M., 2017, MNRAS, 466, 798
Cappellari M., 2022, MNRAS, 526, 3273
Cappellari M., Emsellem E., 2004, PASP, 116, 138
Carnall A. C. et al., 2023a, MNRAS, 520, 3974
Carnall A. C. et al., 2023b, Nature, 619, 716
Carnall A. C. et al., 2024, MNRAS, 534, 325
Ceverino D., Klessen R. S., Glover S. C. O., 2018, MNRAS, 480, 4842
Chabrier G., 2003, PASP, 115, 763
Chapman S. C., Blain A., Ibata R., Ivison R. J., Smail I., Morrison G., 2009, ApJ, 691, 560
Charlot S., Fall S. M., 2000, ApJ, 539, 718
Chartab N. et al., 2020, ApJ, 890, 7
Conroy C., Gunn J. E., 2010, Astrophysics Source Code Library, record ascl:1010.043
Conroy C., Gunn J. E., White M., 2009, ApJ, 699, 486
Cresci G. et al., 2023, A&A, 672, A128
Croft S. et al., 2006, ApJ, 647, 1040
D'Eugenio F. et al., 2024, Nat. Astron., 8, 1443
D'Eugenio F. et al., 2025a, ApJS, 277, 4
D'Eugenio F. et al., 2025b, MNRAS, 536, 51
Daddi E. et al., 2009, ApJ, 694, 1517
Damen M. et al., 2011, ApJ, 727, 1
Davies R. L. et al., 2024, MNRAS, 528, 4976
de Graaff A. et al., 2025, Nat. Astron., 9, 280
Dekel A., Zolotov A., Tweed D., Cacciato M., Ceverino D., Primack J. R., 2013, MNRAS, 435, 999
Donnari M. et al., 2019, MNRAS, 485, 4817
Donnari M., Pillepich A., Nelson D., Marinacci F., Vogelsberger M., Hernquist L., 2021, MNRAS, 506, 4760
Drake A. B. et al., 2020, ApJ, 902, 37
Eilers A.-C. et al., 2024, ApJ, 974, 275
Eisenstein D. J. et al., 2023a, preprint (arXiv:2306.02465)
Eisenstein D. J. et al., 2023b, preprint (arXiv:2310.12340)
Ellison S. et al., 2025, Open J. Astrophy, 8, 12
Eyles L. P., Bunker A. J., Ellis R. S., Lacy M., Stanway E. R., Stark D. P., Chiu K., 2007, MNRAS, 374, 910
Eyles L. P., Bunker A. J., Stanway E. R., Lacy M., Ellis R. S., Doherty M., 2005, MNRAS, 364, 443
Ferland G. J. et al., 2017, Rev. Mex. Astron. Astrofis., 53, 385
Ferruit P. et al., 2022, A&A, 661, A81
Finlez C. et al., 2022, ApJ, 936, 88
Foreman-Mackey D., 2016, J. Open Source Softw., 1, 24
Foreman-Mackey D., Hogg D. W., Lang D., Goodman J., 2013, PASP, 125, 306
Fudamoto Y. et al., 2025, preprint (arXiv:2503.15597)
Gelli V., Pallottini A., Salvadori S., Ferrara A., Mason C., Carniani S., Ginolfi M., 2025, ApJ, 985, 126
Giavalisco M. et al., 2004, ApJ, 600, L93
Glazebrook K. et al., 2017, Nature, 544, 71
Glazebrook K. et al., 2024, Nature, 628, 277
Gordon K. D., Clayton G. C., Misselt K. A., Landolt A. U., Wolff M. J., 2003, ApJ, 594, 279
Guo Y. et al., 2012, ApJ, 749, 149
Gupta A., Yuan T., Tran K.-V. H., Martizzi D., Taylor P., Kewley L. J., 2016, ApJ, 831, 104
Haehnelt M. G., Natarajan P., Rees M. J., 1998, MNRAS, 300, 817
Hainline K. N. et al., 2024, ApJ, 964, 71
Hainline K. N., Hickox R., Greene J. E., Myers A. D., Zakamska N. L., 2013, ApJ, 774, 145
Hamann F. et al., 2017, MNRAS, 464, 3431
Harris C. R. et al., 2020, Nature, 585, 357
Hashimoto T. et al., 2023, ApJ, 955, L2
Helton J. M. et al., 2024a, ApJ, 962, 124
Helton J. M. et al., 2024b, ApJ, 974, 41
Helton J. M., Johnson S. D., Greene J. E., Chen H.-W., 2021, MNRAS, 505, 5497
Hoffman M. D., Blei D. M. Wang C., Paisley J., 2013, J. Mach. Learn. Res., 14, 1303
Hopkins P. F., Hernquist L., Cox T. J., Kereš D., 2008, ApJS, 175, 356
Hunter J. D., 2007, Comput. Sci. Eng., 9, 90
Inskip K. J., Villar-Martín M., Tadhunter C. N., Morganti R., Holt J., Dicken D., 2008, MNRAS, 386, 1797
Ito K. et al., 2024, ApJ, 964, 192
Jakobsen P. et al., 2022, A&A, 661, A80

Ji Z. et al., 2024a, preprint (arXiv:2401.00934)
Ji Z. et al., 2024b, ApJ, 974, 135
Ji Z., Giavalisco M., Williams C. C., Faber S. M., Ferguson H. C., Guo Y., Liu T., Lee B., 2018, ApJ, 862, 135
Johnson B. D., Leja J., Conroy C., Speagle J. S., 2021, ApJS, 254, 22
Johnson B. et al., 2023, dfm/python-fsps: v0.4.4, Zenodo
Jones E., Oliphant T., Peterson P. et al., 2001, http://www.scipy.org/ (last access 12 Aug 2025)
Joye W. A., Mandel E., 2003, in Payne H. E., Jedrzejewski R. I., Hook R. N., eds, ASP Conf. Ser. Vol. 295, Astronomical Data Analysis Software and Systems XII. Astron. Soc. Pac., San Francisco, p. 489
Kashino D., Lilly S. J., Matthee J., Eilers A.-C., Mackenzie R., Bordoloi R., Simcoe R. A., 2023, ApJ, 950, 66
Keel W. C. et al., 2015, AJ, 149, 155
Kennicutt R. C., Evans N. J., 2012, ARA&A, 50, 531
Killi M. et al., 2024, A&A, 691, A52
Kriek M., Conroy C., 2013, ApJ, 775, L16
Kuruvanthodi A., Schaerer D., Marques-Chaves R., Korber D., Weibel A., Oesch P. A., Roberts-Borsani G., 2024, A&A, 691, A310
Lagos C. d. P. et al., 2025, MNRAS, 536, 2324
Leja J., Carnall A. C., Johnson B. D., Conroy C., Speagle J. S., 2019, ApJ, 876, 3
Leja J., Speagle J. S., Johnson B. D., Conroy C., van Dokkum P., Franx M., 2020, ApJ, 893, 111
Lewis A. J. R. et al., 2018, ApJ, 862, 96
Lintott C. J. et al., 2009, MNRAS, 399, 129
Liu G., Zakamska N. L., Greene J. E., 2014, MNRAS, 442, 1303
Liu G., Zakamska N. L., Greene J. E., Nesvadba N. P. H., Liu X., 2013, MNRAS, 430, 2327
Liu W. et al., 2024, ApJ, 976, 33
Liu W. et al., 2025, ApJ, 980, 31
Long A. S. et al., 2020, ApJ, 898, 133
Long A. S. et al., 2024, ApJ, 970, 68
Looser T. J. et al., 2024b, Nature, 629, 53
Looser T. J., D'Eugenio F., Piotrowska J. M., Belfiore F., Maiolino R., Cappellari M., Baker W. M., Tacchella S., 2024a, MNRAS, 532, 2832
Lovell C. C. et al., 2023, MNRAS, 525, 5520
Lu T.-Y., Mason C. A., Hutter A., Mesinger A., Qin Y., Stark D. P., Endsley R., 2024, MNRAS, 528, 4872
Lyu J. et al., 2025, ApJ, 981, L20
Madau P., 1995, ApJ, 441, 18
Marshall M. A. et al., 2023, A&A, 678, A191
Martorano M., van der Wel A., Baes M., Bell E. F., Brammer G., Franx M., Nersesian A., 2024, ApJ, 972, 134
Maseda M. V. et al., 2024, A&A, 689, A73
Miller T. B. et al., 2025, ApJ, 988, 196
Morishita T. et al., 2025, ApJ, 982, 153
Muzzin A., Marchesini D., van Dokkum P. G., Labbé I., Kriek M., Franx M., 2009, ApJ, 701, 1839
Naidu R. P. et al., 2024, preprint (arXiv:2410.01874)
Nanayakkara T. et al., 2024, Scientific Reports, 14, 3724
Nanayakkara T. et al., 2025, ApJ, 981, 78
Neistein E., Dekel A., 2008, MNRAS, 388, 1792
Nelson D. et al., 2019, MNRAS, 490, 3234
Nersesian A. et al., 2024, A&A, 681, A94
Noll S., Burgarella D., Giovannoli E., Buat V., Marcillac D., Muñoz-Mateos J. C., 2009, A&A, 507, 1793
Oesch P. A. et al., 2023, MNRAS, 525, 2864
Oke J. B., Gunn J. E., 1983, ApJ, 266, 713
Onoue M. et al., 2024, preprint (arXiv:2409.07113)
Ormerod K. et al., 2024, MNRAS, 527, 6110
Osterbrock D. E., Ferland G. J., 2006, Astrophysics of gaseous nebulae and active galactic nuclei. University Science Books, Sausalito, California
Oteo I. et al., 2018, ApJ, 856, 72
Pacifici C. et al., 2023, ApJ, 944, 141
Pascalau R.G. et al., 2025, preprint (arXiv:2505.06349)
Pasha I., Miller T. B., 2023, J. Open Source Softw., 8, 5703
Pavesi R. et al., 2018, ApJ, 861, 43
Peng B. et al., 2025, A&A, 694, L1
Peng Y., Maiolino R., Cochrane R., 2015, Nature, 521, 192
Pérez-González P. G. et al., 2005, ApJ, 630, 82
Pérez-González P. G. et al., 2008, ApJ, 675, 234
Pérez-González P. G. et al., 2024, preprint (arXiv:2405.03744)
Perna M. et al., 2023, A&A, 679, A89
Perna M. et al., 2025, A&A, 696, A59
Piotrowska J. M., Bluck A. F. L., Maiolino R., Peng Y., 2022, MNRAS, 512, 1052
Planck Collaboration VI, 2020, A&A, 641, A6
Popesso P. et al., 2023, MNRAS, 519, 1526
Remus R.-S., Kimmig L. C., 2025, ApJ, 982, 30
Rennehan D., Babul A., Moa B., Davé R., 2024, MNRAS, 532, 4793
Riechers D. A. et al., 2010, ApJ, 720, L131
Riechers D. A. et al., 2014, ApJ, 796, 84
Rieke M. J. et al., 2023, ApJS, 269, 16
Robertson B. et al., 2024, ApJ, 970, 31
Ross N. P. et al., 2015, MNRAS, 453, 3932
Rupke D. S. N. et al., 2019, Nature, 574, 643
Salomé Q., Salomé P., Combes F., 2015, A&A, 574, A34
Sandles L. et al., 2023, preprint (arXiv:2307.08633)
Sandles L. et al., 2024, A&A, 691, A305
Saxena A. et al., 2024, MNRAS, 531, 4391
Scholtz J. et al., 2020, MNRAS, 492, 3194
Scholtz J. et al., 2024, preprint (arXiv:2405.19401)
Schreiber C. et al., 2018, A&A, 611, A22
Shen S., Mo H. J., White S. D. M., Blanton M. R., Kauffmann G., Voges W., Brinkmann J., Csabai I., 2003, MNRAS, 343, 978
Silk J., Rees M. J., 1998, A&A, 331, L1
Smolčić V. et al., 2017, A&A, 597, A4
Solimano M. et al., 2025, A&A, 693, A70
Stalevski M., Ricci C., Ueda Y., Lira P., Fritz J., Baes M., 2016, MNRAS, 458, 2288
Stanway E. R. et al., 2004a, ApJ, 604, L13
Stanway E. R., Bunker A. J., McMahon R. G., Ellis R. S., Treu T., McCarthy P. J., 2004b, ApJ, 607, 704
Strait V. et al., 2023, ApJ, 949, L23
Sun F. et al., 2023, ApJ, 953, 53
Sun F. et al., 2024, ApJ, 961, 69
Sun F. et al., 2025, preprint (arXiv:2503.15587)
Taamoli S. et al., 2024, ApJ, 966, 18
Tacchella S. et al., 2022, ApJ, 926, 134 (T22)
Tacchella S., Bose S., Conroy C., Eisenstein D. J., Johnson B. D., 2018, ApJ, 868, 92
Taylor M. B., 2005, in Shopbell P., Britton M., Ebert R., eds, ASP Conf. Seri. Vol. 347, Astronomical Data Analysis Software and Systems XIV. Astron. Soc. Pac., San Francisco, p. 29
Terrazas B. A., Bell E. F., Woo J., Henriques B. M. B., 2017, ApJ, 844, 170
Trager S. C., Worthey G., Faber S. M., Burstein D., González J. J., 1998, ApJS, 116, 1
Trussler J. A. A. et al., 2025, MNRAS, 537, 3662
Trussler J., Maiolino R., Maraston C., Peng Y., Thomas D., Goddard D., Lian J., 2020, MNRAS, 491, 5406
Turner C. et al., 2025, MNRAS, 537, 1826
Umehata H. et al., 2015, ApJ, 815, L8
Valentino F. et al., 2023, ApJ, 947, 20
Valentino F. et al., 2025, A&A, 699, 358
van der Wel A. et al., 2014, ApJ, 788, 28
van Rossum G., 1995, CWI Technical Report, CS-R9526
Vayner A. et al., 2024, preprint (arXiv:2412.02862)
Veilleux S. et al., 2023, ApJ, 953, 56
Venturi G. et al., 2023, A&A, 678, A127
Wang B. et al., 2023a, ApJ, 944, L58
Wang B. et al., 2024, ApJ, 969, L13
Wang F. et al., 2023b, ApJ, 951, L4
Ward E. et al., 2024, ApJ, 962, 176
Weaver J. R. et al., 2023, A&A, 677, A184

Wechsler R. H., Bullock J. S., Primack J. R., Kravtsov A. V., Dekel A., 2002, ApJ, 568, 52
Weibel A. et al., 2024, MNRAS, 533, 1808
Weibel A. et al., 2025, ApJ, 983, 11
Whitaker K. E. et al., 2019, ApJS, 244, 16
Whitler L., Stark D. P., Endsley R., Chen Z., Mason C., Topping M. W., Charlot S., 2024, MNRAS, 529, 855
Withers S. et al., 2023, ApJ, 958, L14
Wu P.-F., 2025, ApJ, 978, 131
Xie L. et al., 2024, ApJ, 966, L2
Yan R., Newman J. A., Faber S. M., Konidaris N., Koo D., Davis M., 2006, ApJ, 648, 281
Yang G. et al., 2022, ApJ, 927, 192
Zamora S. et al., 2024, preprint (arXiv:2412.02751)
Zhu Y. et al., 2025, ApJ, 986, 162

APPENDIX A: LINE FLUXES FROM MULTIBAND PHOTOMETRY

Here, we derive the approximate expressions for the equivalent width EW and line flux $F_{\rm line}$ of an emission line at observed wavelength λ_0, for the two cases where the line is observed in two overlapping filters (equations 1 and 5) or in only one of two overlapping filters (equations 3 and 6). We denote the two filters as 'a' and 'b', their pivot wavelengths as $\lambda_{\rm a}$ and $\lambda_{\rm b}$, and their transmission curves as $t_{\rm a}$ and $t_{\rm b}$. We further define the rectangular filter width as

$$\square_{\rm a} \equiv \frac{1}{T_{\rm a}} \int t_{\rm a}(\lambda) {\rm d}\lambda, \tag{A1}$$

where $T_{\rm a}$ is the maximum of $t_{\rm a}$. We also assume that $t_{\rm a}(\lambda_0)$, the filter transmission at the wavelength of the line, is always approximately equal to $T_{\rm a}$, which unless applies to our observations, but is not necessarily true in general. The spectral flux density can be written as

$$f_\lambda(\lambda) = s(\lambda) + l(\lambda) \tag{A2}$$

where s and l are the flux densities of the continuum and of the emission line, the latter being negligible a few FWHM away from λ_0. The weighted flux density through filter a is

$$F_{\nu,{\rm a}} \equiv \frac{\lambda_{\rm a}^2}{\rm c} \frac{\int t_{\rm a}(\lambda)\,(s(\lambda)+l(\lambda))\,{\rm d}\lambda}{\int t_{\rm a}(\lambda){\rm d}\lambda}. \tag{A3}$$

From the definition of EW, we have

$$EW \equiv -\frac{1}{1+z}\int \frac{l(\lambda)}{s(\lambda)}{\rm d}\lambda, \tag{A4}$$

which we can approximate as

$$EW \approx -\frac{1}{(1+z)t(\lambda_0)}\int \frac{t(\lambda)l(\lambda)}{s(\lambda)}{\rm d}\lambda, \tag{A5}$$

because the *JWST* filters are reasonably well approximated by a top-hat function, and the factor $t(\lambda_0)$ ensures that the transmission value at λ_0 does not change the integral. We now substitute $l(\lambda) = s(\lambda) + l(\lambda) - s(\lambda)$, obtaining

$$EW \approx -\frac{1}{(1+z)t(\lambda_0)}\int \frac{t(\lambda)\,(l(\lambda)+s(\lambda))}{s(\lambda)}{\rm d}\lambda + \frac{\int t(\lambda){\rm d}\lambda}{(1+z)t(\lambda_0)}. \tag{A6}$$

Assuming the continuum to be constant $s(\lambda) = s_0$, we can write

$$EW \approx -\frac{1}{(1+z)t(\lambda_0)s_0}\int t(\lambda)\,(l(\lambda)+s(\lambda))\,{\rm d}\lambda + \frac{\int t(\lambda){\rm d}\lambda}{(1+z)t(\lambda_0)}, \tag{A7}$$

and recalling the definitions of $\square_a$ and $F_{\nu,{\rm a}}$, equations (A1) and (A3), we obtain

$$EW \approx -\frac{{\rm c}\square_{\rm a}T_{\rm a}}{(1+z)t(\lambda_0)\lambda_{\rm a}^2 s_0}F_{\nu,{\rm a}} + \frac{\square_{\rm a}T_{\rm a}}{(1+z)t(\lambda_0)}. \tag{A8}$$

We rearrange for convenience, and substitute $T_{\rm a} \approx t(\lambda_0)$, which is appropriate if the line is well centred in the filter a, and follows from the assumption that the NIRCam filters are approximately shaped as top-hat functions. We thus obtain

$$\frac{(1+z)}{\square_{\rm a}}EW - 1 \approx -\frac{\rm c}{\lambda_{\rm a}^2}\frac{F_{\nu,{\rm a}}}{s_0}. \tag{A9}$$

From here, we can obtain equation (1) by dividing equation (A9) by the corresponding expression for filter b, assuming a and b to be the $F335M$ and $F356W$ filters, and solving for EW. In this case, since we assumed $s(\lambda) = s_0$ to be constant, we also have $\delta_{\rm cont} = 1$. To obtain equation (3), where $F410M$ does not contain the emission line, we can set filter a to be $F444W$, and substitute

$$s_0 = \frac{\rm c}{\lambda_{F410M}^2}F_{\nu,F410M}. \tag{A10}$$

The correction terms for the case of continuum that is constant in f_ν can be obtained by replacing $s(\lambda) = f_0{\rm c}/\lambda^2$. In this case, instead of equation (A9), we obtain

$$\frac{(1+z)}{\square_{\rm a}}EW - 1 \approx -\frac{F_{\nu,{\rm a}}}{F_{\nu,{\rm a,cont}}}, \tag{A11}$$

from which we can derive equations (1) and (3) in a similar fashion as done for the case when the continuum is constant in f_λ.

For the emission-line fluxes, equations (5) and (6), we start again from equation (A3). Assuming the continuum $s(\lambda) = s_0$ to be constant, the first addend can be written as

$$\frac{\lambda_{\rm a}^2}{\rm c}\frac{\int t_{\rm a}(\lambda)s(\lambda){\rm d}\lambda}{\int t_{\rm a}(\lambda){\rm d}\lambda} = \frac{\lambda_{\rm a}^2}{\rm c}s_0. \tag{A12}$$

This term is instead equal to simply s_0 for the case where the continuum s is constant in f_ν, since there would be an additional factor ${\rm c}/\lambda_{\rm a}^2$ that simplifies the original expression. As for the second addend in equation (A3), we have

$$\frac{\lambda_{\rm a}^2}{\rm c}\frac{\int t_{\rm a}(\lambda)l(\lambda){\rm d}\lambda}{\int t_{\rm a}(\lambda){\rm d}\lambda} \approx \alpha_{\rm a}\frac{\lambda_{\rm a}^2}{\rm c}\frac{F_{\rm line}t_{\rm a}(\lambda_0)}{\square_{\rm a}T_{\rm a}} \approx \alpha_{\rm a}\frac{\lambda_{\rm a}^2}{\rm c}\frac{F_{\rm line}}{\square_{\rm a}}. \tag{A13}$$

In these expressions, $\alpha_{\rm a}$ is a space-saving notation, taken to be $\alpha_{\rm a} = 1$ if the emission line is observed in filter 'a', and 0 otherwise.

Summarizing, and considering both filters a and b, we have

$$\begin{aligned} F_{\nu,{\rm a}} &= \alpha_{\rm a}\frac{\lambda_{\rm a}^2}{{\rm c}\,\square_{\rm a}}F_{\rm line} + \frac{\lambda_{\rm a}^2}{\rm c}s_0 \\ F_{\nu,{\rm b}} &= \alpha_{\rm b}\frac{\lambda_{\rm b}^2}{{\rm c}\,\square_{\rm b}}F_{\rm line} + \frac{\lambda_{\rm b}^2}{\rm c}s_0. \end{aligned} \tag{A14}$$

equations (1) and (6) can be obtained from equation (A14) by considering

$$F_{\nu,{\rm a}} - \frac{\lambda_{\rm a}^2}{\lambda_{\rm b}^2}F_{\nu,{\rm b}} = \frac{\lambda_{\rm a}^2}{\rm c}F_{\rm line}\left(\frac{\alpha_{\rm a}}{\square_{\rm a}} - \frac{\alpha_{\rm b}}{\square_{\rm b}}\right) \tag{A15}$$

and solving for $F_{\rm line}$. For equation (5), the filters a and b are $F335M$ and $F356W$, so $\alpha_{\rm a} = 1 = \alpha_{\rm b}$, while for equation (6), a and b are $F444W$ and $F410M$, so $\alpha_{\rm a} = 1$ and $\alpha_{\rm b} = 0$.

APPENDIX B: CENTRE OF THE OVERDENSITY

The sources nearest to the centre of the candidate overdensity form a close group of at least five distinct galaxies, all within 1.5 arcsec from the source JADES-GS-429475. Based on their $z_{\rm phot}$ and location, all these sources belong to the candidate overdensity. JADES-GS-429475 is located 17.5 arcsec (103 pkpc) from the centre of the candidate overdensity. The presence of several galaxies at the same

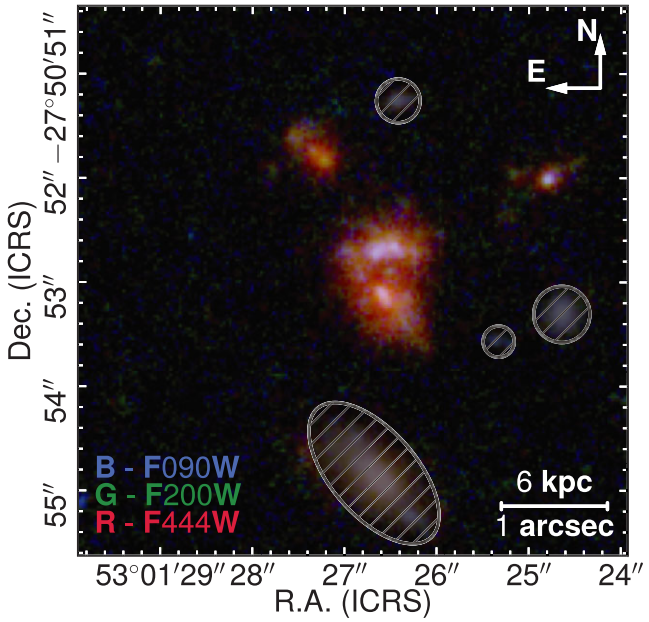

Figure B1. NIRCam false-colour image of the 5-arcsec square near the centre of the candidate overdensity (Fig. 7). We find five galaxies with $z_{\rm phot}$ consistent with the redshift of the overdensity. All these galaxies have positive *F*200*W*–*F*277*W* (Fig. B2c).

redshift and in such a small area of the sky (a square of less than 3-arcsec side, Fig. B1) suggests that the centre of large-scale overdensities may be connected to the formation of massive, early galaxies. We find some evidence for these galaxies being brighter than the typical galaxy at $z \sim 6$ (Fig. B2a; 2.5σ). The fact that all five galaxies have positive *F*200*W*–*F*277*W* colour seems significant, given a sample size of only five (3σ, Fig. B2c). This excess of Balmer-break galaxies may point to older stellar populations, likely due to an earlier start of the SFH.

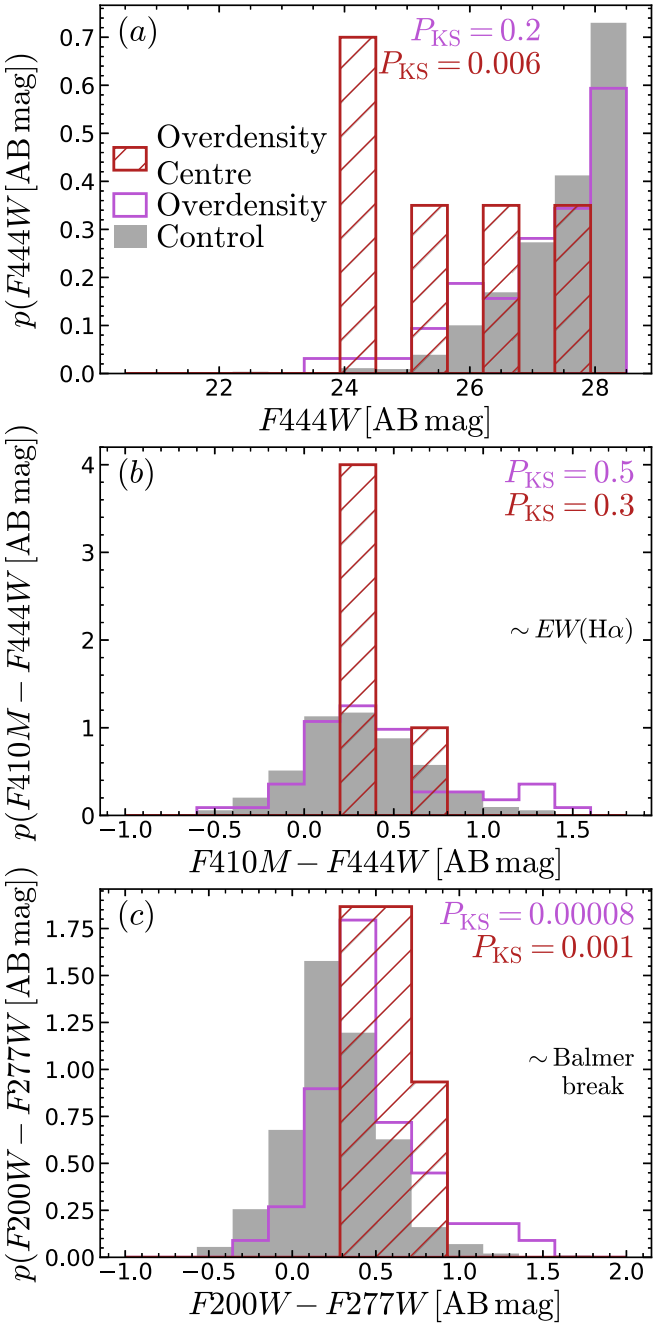

Figure B2. Same as Fig. 8, but also showing the five galaxies nearest to the centre of the overdensity (red hatched histogram). Despite the much smaller sample size, we still find a statistically significant difference in the *F*200*W*–*F*277*W* colour (panel c), pointing to small-scale environment having a distinct effect on the SFH of galaxies.

[1]*Kavli Institute for Cosmology, University of Cambridge, Madingley Road, Cambridge CB3 0HA, UK*
[2]*Cavendish Laboratory – Department of Physics, University of Cambridge, 19 JJ Thomson Avenue, Cambridge CB3 0HE, UK*
[3]*Steward Observatory, University of Arizona, 933 N. Cherry Ave., Tucson, AZ 85721, USA*
[4]*Center for Astrophysics | Harvard & Smithsonian, 60 Garden St, Cambridge, MA 02138, USA*
[5]*Department of Physics and Astronomy, University College London, Gower Street, London WC1E 6BT, UK*
[6]*Centro de Astrobiología (CAB), CSIC–INTA, Cra. de Ajalvir Km. 4, 28850 Torrejón de Ardoz, Madrid, Spain*
[7]*Department of Physics, University of Oxford, Denys Wilkinson Building, Keble Road, Oxford OX1 3RH, UK*
[8]*Scuola Normale Superiore, Piazza dei Cavalieri 7, I-56126 Pisa, Italy*
[9]*Centre for Astrophysics Research, Department of Physics, Astronomy and Mathematics, University of Hertfordshire, Hatfield AL10 9AB, UK*
[10]*Department of Astronomy and Astrophysics, University of California, Santa Cruz, 1156 High Street, Santa Cruz, CA 96054, USA*
[11]*NRC Herzberg, 5071 West Saanich Rd, Victoria, BC V9E 2E7, Canada*
[12]*DARK, Niels Bohr Institute, University of Copenhagen, Jagtvej 155A, DK-2200 Copenhagen, Denmark*
[13]*Center for Frontier Science, Chiba University, 1-33 Yayoi-cho, Inage-ku, Chiba 263-8522, Japan*
[14]*Max-Planck-Institut für Extraterrestrische Physik (MPE), Gießenbachstraße 1, 85748 Garching, Germany*
[15]*NSF National Optical-Infrared Astronomy Research Laboratory, 950 North Cherry Avenue, Tucson, AZ 85719, USA*

This paper has been typeset from a TEX/LATEX file prepared by the author.